REPUBLIC OF TURKEY
ADANA ALPARSLAN TÜRKEŞ SCIENCE AND TECHNOLOGY UNIVERSITY

GRADUATE SCHOOL OF NATURAL AND APPLIED SCIENCES
DEPARTMENT OF BIOENGINEERING

Theoretical Investigation of Mixed Metal Organic Frameworks as H_2 Adsorbents

TUĞÇE GÖKDEMİR
MASTER OF SCIENCE

ADANA, 2022

REPUBLIC OF TURKEY
ADANA ALPARSLAN TÜRKEŞ SCIENCE AND TECHNOLOGY UNIVERSITY

GRADUATE SCHOOL OF NATURAL AND APPLIED SCIENCES
DEPARTMENT OF BIOENGINEERING

Theoretical Investigation of Mixed Metal Organic Frameworks as H_2 Adsorbents

TUĞÇE GÖKDEMİR
MASTER OF SCIENCE

SUPERVISOR
ASSOC. PROF. DR. YELİZ GÜRDAL DURĞUN

ADANA, 2022

I hereby declare that all information in this thesis has been obtained and presented in accordance with academic rules and ethical conduct. I also declare that, as required by these rules and conduct, I have fully cited and referenced all information that is not original to this work.

[Signature]
Tuğçe GÖKDEMİR

ABSTRACT

Theoretical Investigation of
Mixed Metal Organic Frameworks as H_2 Adsorbents

Tuğçe GÖKDEMİR
Department of Bioengineering
Supervisor: Assoc. Prof. Dr. Yeliz GÜRDAL DURĞUN
August 2022, 65 pages

Molecular hydrogen (H_2) is an environmentally friendly, renewable, and sustainable energy carrier. One of the biggest reasons for the limited use of molecular hydrogen (H_2) in energy required applications is the inability to fully develop safe and high-performance hydrogen storage systems. New generation nanoporous materials, in principle, can store H_2 which could be solution of the H_2 storage challenge. Metal Organic Frameworks (MOF), which are new generation nanoporous materials are shown to be promising candidates for the H_2 storage applications. MOFs that contain at least two different metal ions in their structures are called as mixed-metal MOFs (MM-MOF) and they could adsorb H_2 in higher amounts compared to structures containing single metal nodes.

In this thesis, the H_2 adsorption capacities of the 27 MM-MOFs having different topological and chemical features have been theoretically investigated using Grand Canonical Monte Carlo (GCMC) and Density Functional Theory (DFT) simulations. Materials under consideration are divided into two groups. While the 1st group materials have been experimentally synthesized before, the 2nd group materials are hypothetical MM-MOFs designed by You et al. (2020). To the best of our knowledge, H_2 storage performances of the selected MM-MOFs have not been studied in the literature before.

H_2 adsorption isotherms of the MM-MOFs have been predicted by GCMC simulations carried out at 233 K and at pressures between 1 and 100 bar. 5-site (anisotropic) atomic modeling has been used for modeling H_2. The atomic point charges of the MM-MOF atoms required for calculating electrostatic interactions have been determined by applying the DDEC method. Correlation between H_2 storage capacity of the MM-MOFs and their topological and

chemical features have been established and six materials are determined to be the best performing MM-MOFs that can adsorb H_2 both volumetrically and gravimetrically. Electronic structure analysis has been carried out for the top H_2 adsorbing materials by applying DFT simulations.

Keywords: Grand Canonical Monte Carlo Simulations, Density Functional Theory

ÖZET

Çoklu Metal İçeren Metal Organik Kafeslerin H_2 Adsorbanları Olarak Teorik Yöntemlerle İncelenmesi

Tuğçe Gökdemir
Biyomühendislik Anabilim Dalı
Danışman: Doç. Dr. Yeliz GÜRDAL DURĞUN
Ağustos 2022, 65 sayfa

Moleküler hidrojen (H_2) çevre dostu, yenilenebilir ve sürdürülebilir bir enerji taşıyıcısıdır. Enerji gerektiren uygulamalarda moleküler hidrojenin (H_2) sınırlı kullanımının en büyük nedenlerinden biri, güvenli ve yüksek performanslı hidrojen depolama sistemlerinin tam olarak geliştirilememesidir. Yeni nesil nano gözenekli malzemeler, prensip olarak, H_2 depolama sorununun çözümü olabilecek H_2'yi depolayabilir. Yeni nesil nano gözenekli malzemeler olan Metal Organik Kafesler (MOF), H_2 depolama uygulamaları için umut verici adaylar olarak gösterilmektedir. Yapılarında en az iki farklı metal iyonu içeren MOF'lar, çoklu metal MOF'lar (MM-MOF) olarak adlandırılır ve tek metal içeren yapılara göre H_2'yi daha yüksek miktarlarda adsorbe edebilirler.

Bu tezde, farklı topolojik ve kimyasal özelliklere sahip 27 MM-MOF'un H_2 adsorpsiyon kapasiteleri, Grand Kanonik Monte Carlo (GCMC) ve Yoğunluk Fonksiyoneli Teorisi (DFT) simülasyonları kullanılarak teorik olarak araştırılmıştır. İncelenen malzemeler iki gruba ayrılmıştır. 1. grup malzemeler daha önce deneysel olarak sentezlenirken, 2. grup malzemeler You ve ark. (2020) tarafından tasarlanan varsayımsal MM-MOF'lardır. Bildiğimiz kadarıyla, seçilen MM-MOF'ların H_2 depolama performansları daha önce literatürde çalışılmamıştır.

MM-MOF'ların H_2 adsorpsiyon izotermleri, 233 K'da ve 1 ile 100 bar arasındaki basınçlarda gerçekleştirilen GCMC simülasyonları ile tahmin edilmiştir. H_2'yi modellemek için 5 bölgeli (anizotropik) atomik modelleme kullanılmıştır. Elektrostatik etkileşimlerin hesaplanması için gerekli olan MM-MOF atomlarının atomik yükleri DDEC yöntemi uygulanarak belirlenmiştir. MM-MOF'ların H_2 depolama kapasitesi ile topolojik ve kimyasal özellikleri arasında korelasyon kurulmuş ve H_2'yi hem hacimsel hem de gravimetrik olarak yüksek miktarda adsorplayarak en iyi performans gösteren altı adet MM-MOF belirlenmiştir.

DFT simülasyonları uygulanarak H_2'ni en iyi adsorbe edebilen malzemeler için elektronik yapı analizi yapılmıştır.

Anahtar Kelimeler: Grand Kanonik Monte Carlo Simülasyonları, Yoğunluk Fonksiyoneli Teorisi

dedication

This thesis is dedicated to my family.

For their endless love, support, encouragement

ACKNOWLEDGEMENTS

I would like to thank to my supervisor Assoc. Prof. Dr. Yeliz GÜRDAL DURĞUN for her guidance, interest, patience, support, time, and energy. I am extremely lucky to have a supervisor who is knowledgeable, cheerful, and kind. Her desire for research inspires me every time. She introduced me to the world of molecular modeling and simulations and I have learned so much from working with her. This thesis would not be such productive without her motivation and effort.

Furthermore, I am very grateful to my bachelor's degree instructors who are Assoc. Prof. Salih YILMAZ and Dr. Mine TAYKURT DADAY. They always support me whenever I need their help.

I would like to thank to all members of the Molecular Modelling Research Group.

I am very grateful to my dear family members Arslan Murat-Selma-İrfan for their support and help in this thesis and in my life. This thesis is dedicated to you. Especially, I want to express my very gratitude to Arslan Murat who is my dear brother. He always helps me and I always feel his support, although he is far kilometers away from me.

I am very grateful to my dear friend Melih Can OREL who is the best data scientist I have ever met. I took advantages of his computer skills during this period. He always supports, encourages and makes me laugh.

I would like to thank to my dear friends who are İrem DALDABAN, Melissa ÜNALAN, Zerrin ÜNALAN and Lale EREN. I do not have a sister, but thanks to them, I always feel like I have sisters. I am grateful to them for their endless love and support.

I would like to thank to my lovely teammates İpek GÜÇLÜ who always makes me positive and Ayas KİSER who always dances and sings with me. We shared the same office throughout this period and I had so much fun. This process would be really boring without them. We solved a lot of problems together. They are the best teammates I have ever had.

I am very grateful to my colleague Onur İLOĞLU for discussing with me about his experimental study on Metal Organic Frameworks.

I am very grateful to my dear friend Volkan ÇELİK. Whenever I had to solving problems, he was next to me and he supported me during my education.

I would like to thank to my dear best friend Ömer Faruk ERCEYLAN who kept posted me of this master degree position. Moreover, he always cheers me up by making small talks with me.

I would like to acknowledge the Scientific and Technological Research Council of Turkey (TUBITAK). This study has received funding from the TUBITAK under the 1002 Short Term R&D Funding Program (grant agreement No: 120Z160). The calculations reported in this thesis have been performed at the TUBITAK ULAKBIM, High Performance and Grid Computing Center (TRUBA), based in Turkiye.

TABLE OF CONTENTS

TABLE OF CONTENTS ..... **xi**

LIST OF FIGURES ..... **xii**

LIST OF TABLES ..... **xvi**

NOMENCLATURE ..... **xvii**

1. INTRODUCTION **1**

2. LITERATURE REVIEW **8**

2.1. Studies on H_2 storage of Mixed-Metal Organic Framework 14

3. MATERIALS AND METHODS **17**

3.1. Overview on Density Functional Theory 17

3.2. Basic Principles of Grand Canonical Monte Carlo Method 18

3.3. Belof Stern Space (BSS) Model 21

3.4. Assigning Charges for Framework Atoms 22

3.5. Computational Details 23

3.6. Materials 24

4. RESULTS AND DISCUSSIONS **28**

4.1. Modeling MOFs for H_2 Adsorption 28

4.2. Adsorption of Molecular Hydrogen 30

4.3. The Electron Density Difference Maps 39

4.4. Frontier Orbital Analysis 46

CONCLUSIONS **52**

REFERENCES **55**

LIST OF FIGURES

Figure 1.1. Direct biophotolysis process for H_2 production (Nikolaidis & Poullikkas, 2017). **1**

Figure 1.2. Wheelchair with lifter (Wakisaka et al., 1997). **3**

Figure 1.3. Proposed system for H_2 energy cycle. H_2 production from water splitting, H_2 storage device and Fuel cell for producing H_2-based electricity (Schoenung, 2011). **5**

Figure 1.4. Mercedes-Benz F125 which is concept car of Mercedes-Benz brand using H_2 as energy source (Zoellter, 2011). **6**

Figure 2.1. Inorganic, organic building blocks (BB) and a selected framework topology of a) IRMOF-1. b) HKUST-1. Billions of MOFs with different pore structures can be synthesized by combination of various inorganic and organic BB that are favorable with chosen topology (Borboudakis et al., 2017). **8**

Figure 2.2. Structures of IRMOFs which are investigated in Frost et al. study (Frost et al., 2006). **10**

Figure 2.3. (a) Catenated PCN-6 (b) Noncatenated PCN-6′ (Ma et al., 2008). **11**

Figure 2.4. Copper paddle-wheel structure is represented in left. Structure of HKUST-1 is shown in right (Ongari et al., 2017). **13**

Figure 3.1. Summary of bonded and non-bonded interactions. Bonding potentials (left) represent bond, angle bending and torsion from top to bottom where k is a force constant, r_{ij} is the distance between twp particles, θ_{ijk} is the angle between three particles, θ_{ijkl} is the dihedral angle between four (i, j, k, l) particles, equilibrium bond length is represented by r_0 and equilibrium bond angle is represented by θ_0. Non-bonding (right) includes Coulomb and LJ potentials from top to bottom (Dantu, 2012). **20**

Figure 3.2. Ball and stick representations of (a) YOMVIG (b) YOZJEE (c) ZALDUO (d) YEZKOF (e) XUWTAK (f) HEFVAR (g) RUCGOM (h) QIXSOG (i) KALQEV (j) OSOYUR (k) WAVWEW (n) GIFKEL (m) FOKGET (n) UKULOB01 and (o) Cu-Mg-BTC which are modeled in this thesis. **27**

Figure 4.1. Comparison of the gravimetric H_2 adsorption isotherms of the IRMOF-1 up to 100 bar at 298 K obtained by both experiments and the applied BSS model. Red: Simulation results, purple: experimental data from Kaye et al. (2007). **29**

Figure 4.2. Comparison of the gravimetric H_2 adsorption isotherms of the Cu-BTC up to 100 bar at 298 K obtained by experiments and our simulations. Red: Simulation results, purple:

experimental data from Panella et al. (2006), black: experimental data from Li & Yang (2008). 30

Figure 4.3. The gravimetric H_2 adsorption isotherms of the 1st group materials at 233 K. The materials showing large loadings are indicated by colorful closed cycles. The rest of the materials are shown using open blue squares. 31

Figure 4.4. The volumetric H_2 isotherms of the 1st group materials at 233 K. The materials showing large loadings are indicated by colorful closed cycles. The rest of the materials are shown using open blue squares. 32

Figure 4.5. Structures of (a) UKULOB01 (b) UKULOB01 unicell (c) YOZJEE (d) YOZJEE unicell. Fe, Ag, H, C, and N atoms are represented by orange, blue, white, gray, and light blue-magenta respectively. 33

Figure 4.6. The gravimetric H_2 isotherms of the 2nd group materials calculated at 233 K. While top performing ones are shown with colorful closed cycles, the rest of the materials are depicted with open blue squares. 34

Figure 4.7. The volumetric H_2 isotherms of the 2nd group materials calculated at 233 K. 34

Figure 4.8. Gravimetric and volumetric H_2 isotherms of the Co-Mg-BTC calculated at 233 K. 35

Figure 4.9. Enthalpies of adsorption of all MM-MOFs investigated in this thesis. While the materials belonging to the 1st group materials and showing large enthalpies are indicated with colorful cycles, the rest of the 1st group materials are depicted with open blue squares. All the materials belonging to the 2nd group are depicted with open black squares. 36

Figure 4.10. H_2 adsorption sites of (a) YOMVIG (b) QIXSOG (c) OSOYUR (d) Cu-Mg-BTC (e) Fe-Mg-BTC (f) Cr-Mg-BTC. (Al: Ice blue, Co: Purple, P: Tan, O: Red, H: White, Cu: Cyan, N: dark blue, C: Green, Zn: Gray. Mn, Cu, Fe and Cr are represented by ochre in (d), (e), and (f), respectively. 38

Figure 4.11. Electron density difference calculated for the YOMVIG. Isosurfaces taken at + 0.000964 e $Å^{-3}$ for charge accumulation which is represented by pink and -0.000964 e $Å^{-3}$ for charge depletion which is represented by purple. Co, P, Al and O are represented by purple, tan, ice blue, and red, respectively. 40

Figure 4.12. Electron density difference calculated for the QIXSOG. Isosurfaces taken at + 0.00122 e $Å^{-3}$ for charge accumulation which is represented by pink and - 0.00122 e $Å^{-3}$ for charge depletion which is represented by purple. Cu, Mn, N and C are represented by cyan, ochre, dark blue, and green, respectively. 41

Figure 4.13. (a) Electron density difference calculated for the OSOYUR. Isosurfaces taken at +0.00035 e $Å^{-3}$ for charge accumulation which is represented by pink and - 0.00035 e $Å^{-3}$ for charge depletion which is represented by purple (b) polarizations of H_2 molecules. Ca, Zn, H, C and O are represented by ochre, gray, white, green and red, respectively. **42**

Figure 4.14. (a) Electron density difference calculated for the Cr-Mg-BTC. Isosurfaces taken at + 0.001235 e $Å^{-3}$ for charge accumulation which is represented by pink and -0.001235 e $Å^{-3}$ for charge depletion which is represented by purple (b) polarizations of the H_2 molecules. Cr, Mg, H, O and C are represented by ochre, pink, white, red, and green, respectively. **43**

Figure 4.15. (a) Electron density difference calculated for the Fe-Mg-BTC. Isosurfaces taken at + 0.001187 e $Å^{-3}$ for charge accumulation which is represented by pink and -0.001187 e $Å^{-3}$ for charge depletion which is represented by purple (b) Polarizations of H_2 molecules. Fe, Mg, H, O, and C are represented by ochre, pink, white, red and green, respectively. **44**

Figure 4.16. (a) Electron density difference calculated for the Cu-Mg-BTC. Isosurfaces taken at +0.00041 e $Å^{-3}$ for charge accumulation which is represented by pink and -0.00041 e $Å^{-3}$ for charge depletion which is represented by purple (b) Electron accumulations and depletions regions located on the paddle-wheel (c) Polarizations of the H_2 molecules. Cu, Mg, H, O, and C are represented by ochre, pink, white, red and green, respectively. **45**

Figure 4.17. a) HOMO and (b) LUMO representations calculated for the H_2/YOMVIG. Isosurfaces are obtained at the value of ± 0.016505 e $Å^{-3}$. Co, P, Al, and O are represented by purple, tan, ice blue and red respectively. **46**

Figure 4.18. a) HOMO and (b) LUMO representations calculated for the H_2/QIXSOG. Isosurfaces are obtained at the value of ± 0.027494 e $Å^{-3}$. Cu, Mn, N and C are represented by cyan, ochre, dark blue and green, respectively. **47**

Figure 4.19. a) HOMO and (b) LUMO representations calculated for the H_2/OSOYUR. Isosurfaces are obtained at the value of ± 0.022178 e $Å^{-3}$. Ca, Zn, H, C, and O are represented by ochre, gray, white, green and red, respectively. **48**

Figure 4.20. a) HOMO and (b) LUMO representations calculated for the H_2//Cr-Mg-BTC. Isosurfaces are obtained at the value of ±0.018 e $Å^{-3}$. Cr, Mg, H, O and C are represented by ochre, pink, white, red and green, respectively. **49**

Figure 4.21. a) HOMO and (b) LUMO representations calculated for the H_2//Fe-Mg-BTC. Isosurfaces are obtained at the value of ± 0.021719 e $Å^{-3}$. Fe, Mg, H, O, and C are represented by ochre, pink, white, red, and green, respectively. **50**

Figure 4.22. a) HOMO and (b) LUMO representations calculated for the H_2//Cu-Mg-BTC. Isosurfaces are obtained at the value of ± 0.018 e $Å^{-3}$ **.** Cu, Mg, H, O and C are represented by ochre, pink, white, red, and green, respectively. **51**

LIST OF TABLES

Table 3.1. Parameters of the BSS model (Franz et al., 2018). **22**

Table 3.2. 1st group of MM-MOFs investigated in this thesis. Void fractions, pore limiting diameters (PLD), the largest cavity diameters (LCD) and atoms in the structures are reported (*Metal Organic Framework Database | Mofs*, n.d.). **26**

Table 3.3. 2nd group of 11 MM-BTCs investigated in this thesis. Void fractions, PLD, LCD and atoms in the structures are reported (You et al., 2020). Co-Mg-BTC material is created by us in order to examine the effect of the presence of the Co on H_2 loading. **26**

Table 4.1 Experimental data of the gravimetric H_2 adsorption measured at 1 bar and 77 K for IRMOF-1. The results of our calculations are also reported. **29**

Table 4.2. Measured distances between metal sites and H_2 molecules which are provided in Å. Geometry optimizations are carried out for the selected GCMC snapshots. **38**

Table 4.3. Top performing MM-MOFs from the 1st and 2nd group materials investigated in this thesis. Void fraction, PLD, LCD and metal sites of the MM-MOFs are reported. Gravimetric (wt %) and volumetric (g/L) H_2 uptake and enthalpies of adsorptions are calculated at 233 K and 100 bar. **39**

NOMENCLATURE

DOE	: United States Department of Energy
MOFs	: Metal Organic Frameworks
HFTO	: The Hydrogen and Fuel Cell Technologies Office
MM-MOFs	: Mixed Metal Organic Frameworks
BDC	: Benzenedicarboxylate
BTC	: Benzene-1,3,5-tricarbocylate
LJ	: Lennard-Jones Potential
GCMC	: Grand Canonical Monte Carlo
MC	: Monte Carlo
DFT	: Density Functional Theory
DDEC	: Density Derived Electrostatic and Chemical Charges
HKUST	: Hong Kong University of Science and Technology
MIL	: Material from Institut Lavoisier
T	: Temperature
UFF	: Universal Force Field
BSS	: Belof-Stern-Space
DL	: Darkrim-Levesque
PLD	: Pore limiting diameter
LCD	: Largest cavity diameter
Q	: Canonical partition function
p_i	: Probability of a system in an i^{th} state
p(r)	: Probability of density
IRMOFs	: Isoreticular metal–organic frameworks
Å	: Angstrom
H_2	: Molecular hydrogen
H	: Hydrogen
r	: Coordination of particles
Si	: Silicon
Ga	: Gallium

Al	: Aluminum
N	: Nitrogen
Cu	: Copper
Co	: Cobalt
Ca	: Calcium
Zn	: Zinc
Mn	: Manganese
Cd	: Cadmium
W	: Tungsten
Ba	: Barium
Be	: Beryllium
P	: Phosphorus
Mg	: Magnesium
Pt	: Platinum
Rh	: Rhodium
Au	: Gold
Ag	: Silver
Cr	: Chromium
O	: Oxygen
Li	: Lithium
Cl	: Chlorine
Ti	: Titanium
Mo	: Molybdenum
Ru	: Ruthenium

1. INTRODUCTION

Endangered natural resources and greenhouse emissions result in serious concerns for sustainable development. Usage of fossil fuels leads to global warming, economic dependency, air and environmental pollution problems (Nazir et al., 2020; Niaz et al., 2015). Therefore, a wide range of research boosting have been conducted on climate change, alternative or advanced fuels, as well as renewable energy resources. It is supposed that world population could rise to nearly ten billion in 2050 and nearly eleven billion around in 2100 stated by United Nations *(United Nations Department of Economic and Social Affairs, n.d.).* Thus, large increment of energy need is expected in worldwide. Providing growing energy demand from sustainable and eco-friendly sources is essential for fighting against global warming.

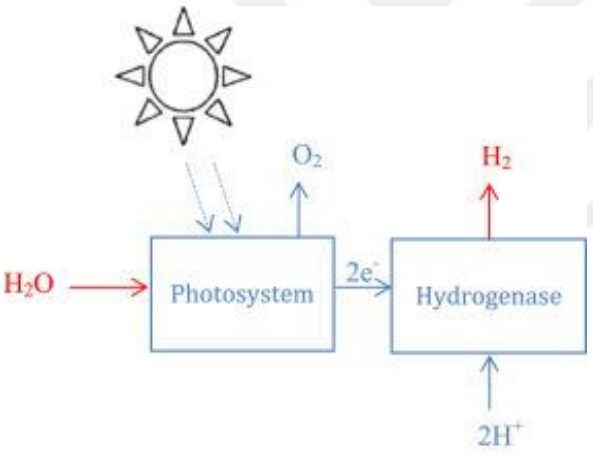

Figure 1.1. Direct biophotolysis process for H_2 production (Nikolaidis & Poullikkas, 2017).

Molecular hydrogen (H_2) can be produced from wide range of resources (biological resources, fossil fuels, etc.). H_2 production can divided into two groups which are conventional and renewable technologies according to resource used in the process. Conventional technologies are based upon processing of fossil fuels and concerning the renewable technologies the H_2 is produced by renewable sources, such as biomass or photocatalytic splitting of water. Biomass can be obtained from plant or animal waste, e.g., energy crops and crop residues, wood from forests and forest residues, grass, industrial residues, animal and municipal waste. Biomass process includes thermochemical or biological processes. Biological process is commonly operated at ambient conditions and also waste recycling is provided during this process by usage of waste materials (Nikolaidis & Poullikkas, 2017). One of

example which is the direct biophotolysis for biological process is given in Figure 1.1. Water molecules split to hydrogen ion and oxygen by green algae. This stage is carried out by photosynthesis. Light is captured by photosynthetic apparatus. Transformation of hydrogen ion to hydrogen gas occurs via hydrogenase enzyme (Nikolaidis & Poullikkas, 2017). O_2 and H_2 are obtained at the end of the process (You-Kwan et al., 2013). The reaction of this process is shown below (Nikolaidis & Poullikkas, 2017).

$$2H_2O + \text{light energy} \rightarrow 2H_2 + O_2$$

Usage of hydrogen as a next generation fuel in automotive and energy applications has become a crucial research area because H_2 has a larger energy density in comparison with gasoline and only water vapor released to environment when H_2 is burned, thus H_2 is an eco-friendly alternative to fossil fuels (Niaz et al., 2015; Park et al., 2012). Today, one of the major factors of obstructing to have a wide application area of H_2 energy is the inability to fully develop safe and efficient H_2 storage systems. Development of H_2 (energy) storage systems plays a major role in satisfying the growing energy demand and fighting against climate change in worldwide.

European Green Deal targets to reduce net greenhouse gas emissions to zero by 2050 *(A European Green Deal, n.d.).* To achieve this goal, energy conversion is required in the transportation sector and industry. H_2 is a key priority to achieve the aim of European Green Deal. Overcoming H_2 storage barrier will help to facilitate H_2 energy usage, develop corresponding technologies, and increase life standards of the society. European Union (EU) plans to increase the share of H_2 in Europe's energy mix from the current less than 2% to 13-14% by 2050. *(Hydrogen Strategy, n.d.)* The global effort has been the basis for distributing, storing and dispensing H_2 at large volumes and over long distances.

H_2 can be used as a power and electricity supply as well as for cooling and heating. Therefore, the application area of H_2 is, indeed, wide (Yusaf et al., 2022). H_2 has been already using in rockets for National Aeronautics and Space Administration (NASA) (Winarta et al., 2020). H_2 energy can be also preferred for personal uses such as mobile phones, watches, computers, calculators, etc (Jain, 2009). Also, H_2 can be used in natural gas pipelines by blending. Heating and cooking have been supplied by blend of H_2 (up to 20%) in a village of England (HyDeploy Project) *(Bloomberg, n.d.).* By 2030, the aim of U.K. is to have the first town to utilize 100% H_2. Currently, blend of H_2 and natural gas have been reaching 668 houses, a school and number of small businesses. It is a good example for decarbonization of industry

and homes. This application for sure, will help to provide carbon neutrality of U.K. by 2050 *(HyDeploy, n.d.)*.

H_2 energy can be also used in medical applications. There are, indeed, applications of H_2 adsorbent alloys used in medical and rehabilitation equipment (Wakisaka et al., 1997). The metal hydride actuators can be used in lifters for disabled people such as toilet lifter, toilet seat lifter, wheelchair with lifter, see Figure 1.2 (Wakisaka et al., 1997). Metal hydride alloy can adsorb and desorb H_2 (Sasaki et al., 1987). Reaction between metal hydride alloy and H_2 produces metal hydride and produced heat is converted to mechanical energy in a sealed container system (Ino et al., 2009). Reversible reaction of H_2 absorbing alloy is used in metal hydride actuators (Wakisaka et al., 1997).

Figure 1.2. Wheelchair with lifter (Wakisaka et al., 1997).

Increase of H_2 storage capacity under the applicable conditions would develop technologies that use H_2 energy. H_2 storage has significant challenges, especially for the automotive industry. The "safe and efficient storage" of eco-friendly H_2 energy is a critical point. High-pressure storage tanks are expensive and have explosion risks. On the other hand, storing H_2 as a liquid is expensive and has also security concerns. In this method of storing, H_2 is kept at cryogenic temperatures because of the boiling point of H_2 (21K at atmospheric pressure) (Basdogan & Keskin, 2015; Sagara et al., 2004). Development of storage technology which does not require cryogenic temperatures and high pressures is important for overcoming H_2 storage challenge (Lin et al., 2008).

H_2 storage is divided into two categories which are physical-based and material-based by United States Department of Energy (DOE) *(Hydrogen and Fuel Cell Technologies Office,*

n.d.). Physisorption process is based on absorption of H_2 onto the surface of the highly porous material by van der Waals interactions (Abe et al., 2019; Niaz et al., 2015). Metal hydrides are examples of promising materials storing H_2, however they are heavy and high-priced (Sagara et al., 2004). These types of obstacles have led to search for new storage materials which are light and cheap.

Metal Organic Frameworks (MOFs), have been investigated as potential H_2 storage materials. MOFs which are new generation nanoporous materials include metal atoms and organic ligands that bind metal atoms together. MOFs are coordination compounds and have transition metals in their structures such as Zn, Cu, Co, etc. Fuel cells, supercapacitors, and catalytic conversions are examples of energy implementations of MOFs (Furukawa et al., 2013). Fuel cells are next-generation devices that are using H_2 source as energy by converting chemical energy to electrical energy (X. Li et al., 2020). An example system for using H_2 energy is shown in Figure 1.3. Electrolyzer is used to convert water to H_2, then H_2 is stored using an appropriate material. Stored H_2 can be recharged and supplied to the fuel cell to produce electricity (Schoenung, 2011).

One of the major reasons for the lack of usage of eco-friendly H_2 as a fuel is that it has not stored at high density under the applicable circumstances yet (Torres et al., 2018). The Hydrogen and Fuel Cell Technologies Office (HFTO) is working on development of onboard automotive hydrogen storage systems that have driving range more than 300 miles. Conditions are determined as 233 K-333 K and 5-12 bar (2020 DOE target: 0.045 kg H_2/kg system in gravimetric capacity and 0.030 kg H_2/L system in volumetric capacity) *(DOE Technical Targets for Onboard Hydrogen Storage for Light-Duty Vehicles, n.d.).* Parameters which are price, safety, efficiency, and performance requirements are considered for onboard automotive hydrogen storage systems *(Hydrogen Storage, n.d.).*

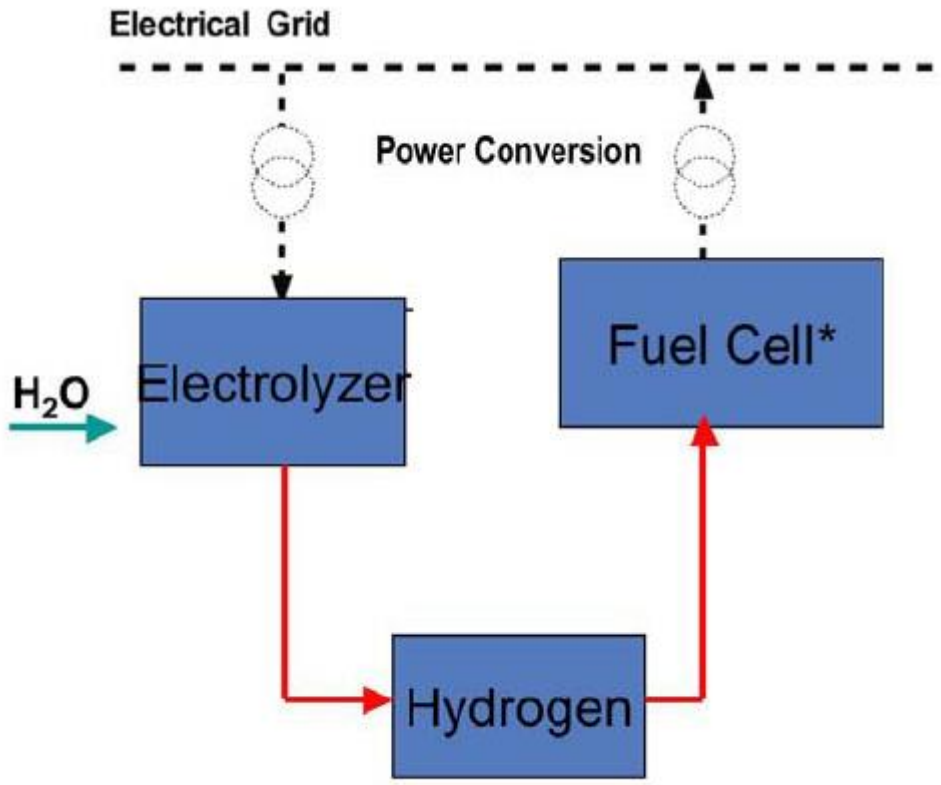

Figure 1.3. Proposed system for H_2 energy cycle. H_2 production from water splitting, H_2 storage device and Fuel cell for producing H_2-based electricity (Schoenung, 2011)**.**

At the present time, famous automotive brands tend to produce vehicles that use alternative and renewable fuels instead of fossil fuels. Some vehicle brands have already been producing car models which are using H_2 as fuel. Toyota brand's Mirai has H_2 fuel cell and is zero-emission vehicle. Mirai is a prominent example of automotives using H_2 energy *(Hidrojen Yakıtlı Toyota Mirai'den Dünya Menzil Rekoru, n.d.)*. Development of new generation of nanoporous materials that can store H_2 (energy) is important for development of these type of vehicles which can use new generation of H_2 fuel. H_2, which is used as a fuel in the automotive industry, should be stored in light materials and in applicable temperature and pressure. Also, storage materials should have small volume, and, fast charging kinetic (Zeleňák & Saldan, 2021). Investigation of MOFs has major priority in order to achieve these conditions successfully. It is envisaged that MOFs can provide safe and efficient H_2 storage in automotive applications. Mercedes-Benz brand will adopt MOF-5 as storage medium in their Mercedes-Benz F12 which is a concept car (Clark, n.d.; Furukawa et al., 2013). The Mercedes-Benz F125 is shown in Figure 1.4 (Zoellter, 2011). The increase in the H_2 storage capacities of MOFs leads to common use of these materials as H_2 storage media in vehicles. All efforts for improving H_2

storage will expand usage of H_2 fuel cells in not only cars but also trucks, buses, and marine vessels (Zohuri, 2018).

Figure 1.4. Mercedes-Benz F125 which is concept car of Mercedes-Benz brand using H_2 as energy source (Zoellter, 2011).

There are wide range of researches in literature on MOFs having single type metal. Various design, synthesis, and, post-synthesis modification studies are carried out both experimentally and theoretically in order to improve the H_2 storage capacity of single-metal MOFs. However, studies on H_2 storage capacities of Mixed-metal MOFs (MM-MOFs) are relatively carried out less (Peedikakkal & Aljundi, 2020). MOFs having two different or more than two different metal ions in their structures are called as mixed-metal MOFs (Abednatanzi et al., 2019; Masoomi et al., 2019). Open metal sites can increase the enthalpy of adsorption and H_2 storage capacity (Abednatanzi et al., 2019; Kapelewski et al., 2018; Sule et al., 2021). MM-MOFs offer open/unsaturated metal sites which are able to strongly interact with H_2 (Suh et al., 2012; Winarta et al., 2020). In this way, MM-MOFs have the potential to achieve high H_2 storage even at ambient temperatures. Nearly 15 kJ/mol value of isosteric heat of H_2 adsorption can enough for ideal H_2 storage at ambient temperatures (Bhatia & Myers, 2006; Sule et al., 2021). Obtaining H_2 binding enthalpies between -15 to -20 kJ/mol can enhance H_2 storage at favorable conditions in light-duty fuel cell vehicles (Kapelewski et al., 2018).

In this thesis, two groups of materials are selected and their H_2 storage performances have not been investigated so far. First group offers differences in terms of metal diversity and chemical/topological properties. The second group of the materials are hypothetical and formed by addition and combination of different transition metals into the structures.

The aim of this thesis is to theoretically investigate H_2 adsorption capacities of selected MM-MOFs which have different topological and chemical properties by applying Grand Canonical Monte Carlo (GCMC) and Density Functional Theory (DFT) methods. Both gravimetrically and volumetrically, the best H_2 adsorption MM-MOFs are determined and further investigations are carrying out using quantum-mechanical calculations for the best performing MM-MOFs. This thesis makes differences to the literature in terms of the investigated materials as well as the applied theoretical methods, for example the charges of the atoms of the MM-MOFs are determined by more accurate DFT-based method as well as rather complicated Belof-Stern-Space (BSS) model is used for modeling H_2 which is an anisotropic and five-site charge–quadrupole model.

Following this introduction, literature Review chapter includes and criticizes the experimental and computational studies on H_2 storage of MM-MOFs in the literature. A brief information on GCMC and DFT methodologies as well as the properties at the selected MM-OFs are given in the materials and method section. Performances of MM-MOFs are introduced and discussed in the Results and Discussions chapter. Conclusion chapter includes a brief summary at the key results as well as future prospects. Besides, a correlation between H_2 storage capacity of the MM-MOFs and their topological/chemical features will be established. This thesis will help development of new-generation H_2 storage materials as well as, provide valuable information on design of new MM-MOFs.

2. LITERATURE REVIEW

This section reviews experimental and computational studies on H_2 storage performances of MM-MOFs. The main focus is the sorption properties of MM-MOFs having open metal sites.

MOFs have large surface areas varying between 1000 and 10000 m^2/g. They have high porosity ranging from 10% to 90% and their densities vary between 0.2 and 1 g/cm^3 (Kumar et al., 2020). MOFs have high thermal and mechanical stability and MOF synthesis can be considered as inexpensively . As an example of MOFs, the MOF-5 (also called IRMOF-1) is the most popular MOF that have been studied in the literature, see Figure 2.1. MOF-5 has Zn ion connected through 1,4-BDC (benzenedicarboxylate) organic ligands and has large pore size distribution (10.9/14.3 Å) (Gurdal & Keskin, 2012).

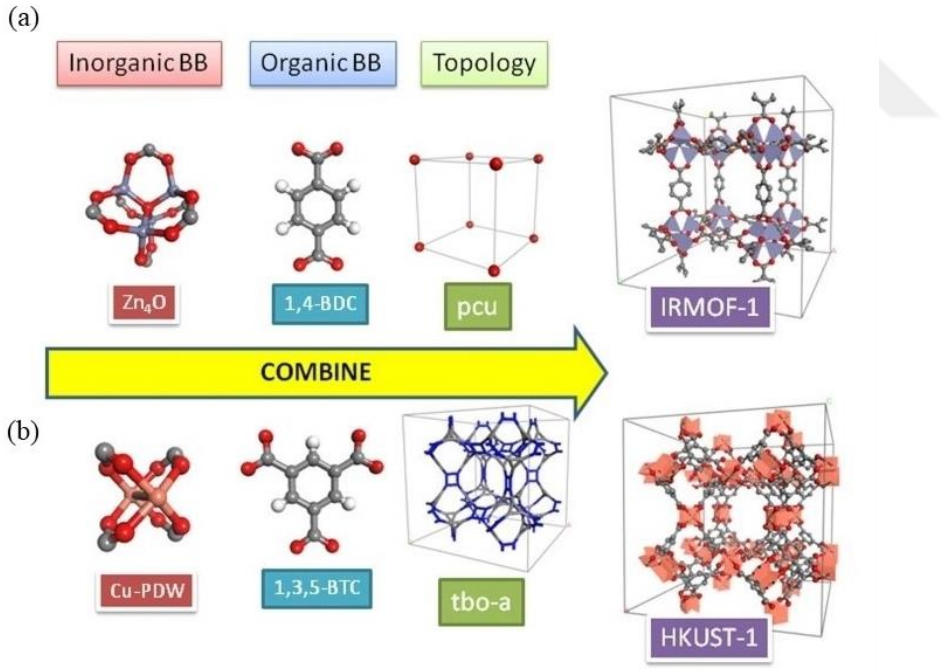

Figure 2.1. Inorganic, organic building blocks (BB) and a selected framework topology of a) IRMOF-1. b) HKUST-1. Billions of MOFs with different pore structures can be synthesized by combination of various inorganic and organic BB that are favorable with chosen topology (Borboudakis et al., 2017).

MOFs offer wide range design preferences, since they can be functionalized by adding many different chemical groups to their organic ligands. They also possess wide variety of transition metals in their structures. MOFs have tunable pore sizes and surface areas, thus they can be designed for a specific application (Liu et al., 2020). Application areas of MOFs can be listed as drug delivery, gas storage and separation, sensors, and, catalysis. Tunable chemical and topological properties as well as their large surface area and high porosity enable MOFs to be used in H_2 storage applications (Collins & Zhou, 2007; Li et al., 2018).

H_2 storage performances of the MOFs has been investigated for the first time in 2003 by Yaghi et al. (Hu & Zhang, 2010; Rosi et al., 2003). According to the results, at 78 K and 0.8 bar H_2 uptake of MOF-5 was measured as 4.5 wt% (Rosi et al., 2003). Another study on H_2 storage of MOFs carried out by Ferey et al. in 2003. They investigated the H_2 capacity of MIL-53 which is $M(OH)[C_6H_4(CO_2)_2]$ ($M=Al^{3+}$, Cr^{3+}; MIL: material from Institut Lavoisier). MIL-53 has stored H_2 3.2 wt % (M=Cr) and 3.8 wt % (M=Al) at 77 K and under 16 bar pressure (Férey et al., 2003). The early studies on H_2 storage capacities of MOFs have shown promising results (Hirscher & Panella, 2007), however strategies and new design methodologies, e.g. high porosity with appropriate pore sizes, impregnation, catenation, open metal sites, MOFs with light metals, and functionalized linkers have been arisen in order to adsorp H_2 using energy friendly operating conditions, such as at room temperature conditions or lower pressures (Han et al., 2009). For instance, studies have shown that MOFs having smaller pore sizes can increase H_2 storage capacity by increasing interactions between H_2 molecules and pore walls as well as the degree of confinement of the H_2 molecules (Lin et al., 2012). Smaller pores are advantageous for H_2 storage as it requires strong interaction between MOF and H_2 (Bobbitt et al., 2016). Generally, the optimal pore size is 4.5–5 Å which allows more interaction between framework and the H_2 for H_2 storage. Also, 2.8–3.3 Å pore sizes which are close to the H_2 kinetic diameter (~ 2.8 Å) are ideal (Collins & Zhou, 2007).

Masika and Mokaya (2012) studied impact of different pore sizes on the H_2 adsorption for porous carbons which have similar surface. In principle, materials having smaller pore size possess larger surface area and materials having larger pore sizes possess smaller surface area Experiments have been carried out at 77 K and 20 bar. The excess (total) H_2 adsorption of carbon materials which have similar surface area, 3340 m^2/g, are measured as 3.7 (5.4) wt% for materials having pore size around 31 Å, 4.8 (6.3) wt% for materials having 23 Å pore size and 6.3 (7.3) wt% for materials having pore size around 12 Å. The excess (total) H_2 adsorption of carbon materials which have similar surface area as 2770 m^2/g are reported as 1.7 (3.0) wt%

for a material having pore size as 28 Å, and 5.6 (6.4) wt% for a material having 15 Å pore size. Results suggest that H_2 adsorption of carbon materials can be enhanced by using materials possessing larger surface areas and smaller pore sizes.

Frost et al. (2006) carried out Grand canonical Monte Carlo (GCMC) simulations for investigating effects of surface area, free volume, and heat of adsorption on H_2 uptake of isoreticular metal–organic frameworks (IRMOFs), see Figure 2.2, at wide range of pressures. Framework topology and surface chemistry are same for IRMOFs under consideration, however their pore size distributions differ. They classified H_2 uptake into three different groups according to obtained results. H_2 uptake is related with; heat of adsorption at low pressures (0.1 bar), surface area at intermediate pressures (30 bar) and free volume at larger pressures (120 bar). IRMOF-4 shows higher heat of adsorption (7.2 kJ/mol) which is attributed to material's small pore sizes and alkyl chains providing large number of atoms that can attract molecular hydrogens. Interaction between H_2 and pore surfaces of IRMOFs-1, -4, -6, and -7 are higher due to their small pore sizes. Small pore size, on the other hand, leads to lower free void spaces. IRMOF-16 shows higher adsorption above 15 bar. Void fractions of IRMOFs-1, -4, -6, -7 and -16 are 0.780, 0.597, 0 .745, 0.718, and 0.905, respectively.

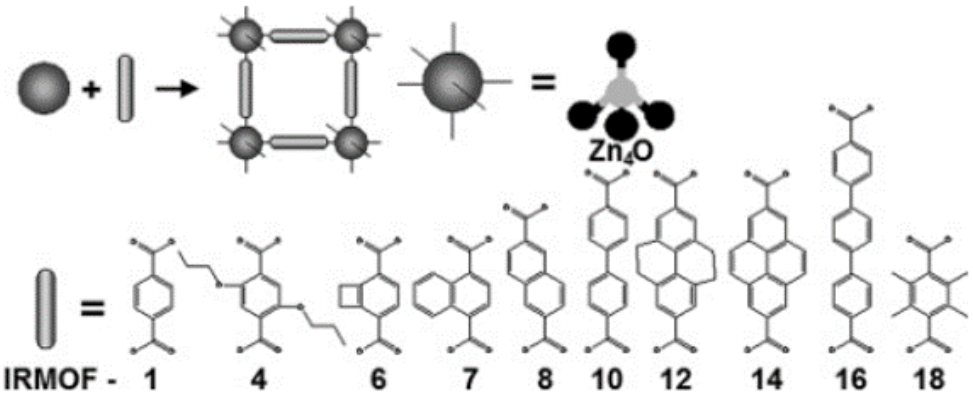

Figure 2.2. Structures of IRMOFs which are investigated in Frost et al. study (Frost et al., 2006).

Volumetric uptake of H_2 generally decreases by increasing pore sizes, however gravimetric uptake of H_2 increases for materials having larger pore sizes (Han et al., 2009). Impregnation methods can increase volumetric uptake by insertion of another adsorbate inside the MOFs having large pores (Han et al., 2009; Rowsell & Yaghi, 2005). In this way, extra surface area is created and also heat of adsorption is increased (Lai et al., 2015).

Pore sizes can also be tuned by catenation. Catenation is separated into two forms which are interpenetration and interweaving. Interpenetration is maximum displacement of

frameworks from each other and interweaving including many close contacts is minimal displacement of frameworks from each other (Rowsell & Yaghi, 2005). Catenation offers not only smaller pore size but also double number of metal-corner sites by second framework (Ryan et al., 2008). Ma et al. (2008) synthesized catenated and noncatenated forms of PCN-6 which have formula of $Cu_3(TATB)_2$ (TATB = 4,4′,4″-s-triazine-2,4,6-triyl-tribenzoate with a formula of $C_{24}H_{12}N_3O_6$) and investigated their H_2 uptakes (Ma et al., 2008). Catenated and noncatenated (PCN-6′) are shown in Figure 2.3. They carried out H_2 sorption measurements up to 50 bar at 77 and 298 K. Isosteric heat of adsorption of PCN-6 is reported as 6.2-4.5 kJ/mol and PCN-6′ is 6.0-3.9 kJ/mol. They attributed increment of isosteric heat of adsorption to smaller pore size of PCN-6 resulted due to catenation. Also, their Inelastic Neutron Scattering (INS) studies showed that PCN-6 has three specific H_2- binding Cu sites and PCN-6′ has one specific H_2-binding Cu site. The excess gravimetric and volumetric H_2 adsorption of PCN-6 are measured as 6.7 wt% and 40.2 g/L while excess gravimetric and volumetric H_2 adsorption of PCN-6′ are reported as 4.0 wt% and 11.8 g/L at 77 K and 50 bar. Excess H_2 adsorption performance of PCN-6 (0.92 wt %) is better than PCN-6′ (0.40 wt %) at 298 K and 50 bar as well. They connected this improvement of H_2 adsorption with larger surface area and smaller pore size (9.0 Å) Also, their previous study showed that Langmuir surface area of PCN-6 and PCN-6′ are 3800 m^2/g and 2700 m^2/g, respectively. They observed that 29% increase in excess gravimetric hydrogen uptake at 77 K and 1 bar and a 133% increase in volumetric hydrogen uptake by catenation (Ma et al., 2007).

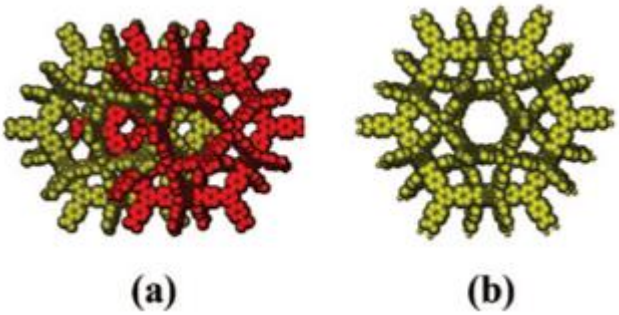

Figure 2.3. (a) Catenated PCN-6 (b) Noncatenated PCN-6′ (Ma et al., 2008).

Bobbitt et al. (2016) investigated H_2 adsorption capacities of 137,000 hypothetical MOFs applying GCMC simulations at 77 K and at 100 bar (loading) and 2 bar (desorption). According to their results, the optimum pore size maximizing H_2 adsorption at 77 K is determined as 12-15 Å, however, this value is greater than the optimum pore size value maximizing H_2 adsorption at room temperature. The MOF which shows the greatest volumetric

deliverable capacity (50 g/L) possesses 0.9 void fraction and 14.25 Å the largest cavity diameter (LCD). One another MOF which shows the best gravimetric deliverable capacity (24.6 wt%) possesses 0.93 void fraction and 24.75 Å LCD.

Replacement of heavy atoms with lighter atoms, such as replacement of Zn^{2+} with Be^{2+}, can increase gravimetric hydrogen uptake in the framework (Lai et al., 2015). Volumetric H_2 adsorption capacity and H_2 physisorption energy can be also improved by functionalization of organic linkers (Han et al., 2009; Lai et al., 2015). MOFs commonly possess aromatic backbones, e.g., benzene and naphthalene (Han et al., 2009). Ab initio calculations carried out so far show proof that interaction between H_2 and aromatic linkers can be increased by addition of $–NH_2$, –OH and $–CH_3$ groups (Han et al., 2009; Rowsell & Yaghi, 2005). Benzene has 3.91 kJ/mol binding energy, while additional $C_6H_5NH_2$, $C_6H_5CH_3$, and C_6H_5OH linkers result in 4.52 kJ/mol, 4.40 kJ/mol, 4.00 kJ/mol binding energies, respectively. This additional groups can enhance the aromatic system electronically. H_2 storage can be improved by functionalization of organic linkers at low temperatures. However, this process might decrease the storage at high temperatures due to decreasing pore sizes (Han et al., 2009). Sagara et al. investigated binding energies of IRMOF-1, IRMOF-3, IRMOF-6, IRMOF-8, IRMOF-12, IRMOF-14, IRMOF-18, and IRMOF-993 by high-quality second-order Møller–Plesset (MP2) calculations. According to their results, addition of NH_2 or CH_3 to each linker can improve binding energy. IRMOF-3 linker which is produced by IRMOF-1 linker including additional NH_2 group has 4.72 kJ/mol binding energy. 4.86 kJ/mol binding energy is obtained by addition of C_2H_4 group to the original BDC linker (IRMOF-6) and 4.54 kJ/mol is obtained by addition of a benzene ring to the original BDC linker (IRMOF-8). 5.42 kJ/mol binding energy is obtained by addition of four CH_3 groups (IRMOF-18).

Another method that can increase the H_2 storage capacity is incorporation of open metal sites in the structure. In this way, stronger interaction between unsaturated metal atoms and H_2 molecules are obtained (Lin et al., 2012). Open metal sites can be existed when there are vacant Lewis acid sites on metal ions. In short, not fully coordinated metal ions in the framework are called as open metal sites. The open metal sites are also known as coordinatively unsaturated sites or open coordination sites. Open metal sites were firstly reported for HKUST-1 (HKUST = Hong Kong University of Science and Technology), also known as Cu-BTC, which has open Cu^{2+} sites. Dicopper paddle-wheel unit are linked by trigonal 1,3,5-btc (H_3btc = 1,3,5-benzentricarboxylate) linkers in HKUST-1 (Kökçam-Demir et al., 2020). Structure of HKUST-1 (right) and Cu^{2+} paddle wheel (left) is shown Figure 2.4.

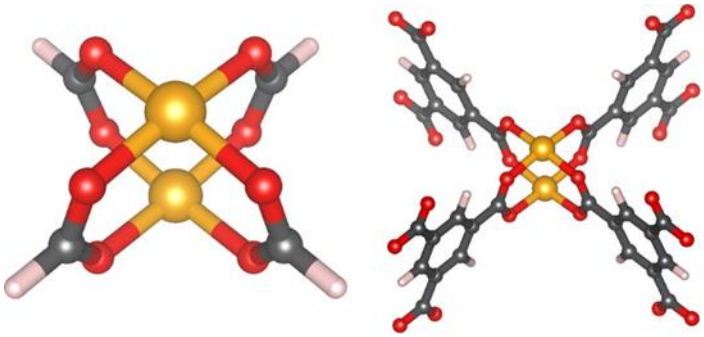

Figure 2.4. Copper paddle-wheel structure is represented in left. Structure of HKUST-1 is shown in right (Ongari et al., 2017).

First theoretical research on the effect of open metal sites on H_2 adsorption performances of MOFs have been carried out by Yang and Zhong (2006) (Han et al., 2009). They applied GCMC and DFT simulations in order to investigate preferable H_2 adsorption sites of MOF-505 having unsaturated Cu^{2+} sites. They used 3-site H_2 model including diatomic molecule with Lennard-Jones (LJ) core and partial charges on each H atom as well as on the dummy atom (point charges are 0.468 e, -0.936 e, 0.468 e). Feynman-Hibbs potential have been applied in order to take dispersion interactions into account. The adsorption energy is calculated as -13.44 kJ/mol, which is high and attributed to the presence of the open metal sites in the framework.

MM-MOFs containing open metal sites have been shown to possess higher heat of adsorption than MOFs having single type metal atoms in their structures (Getman et al., 2012). Kubas-type interactions are important for MOFs with open metal sites. These interactions which arise due to the bonding between d orbitals of the transition metals and H_2 atoms are, generally, stronger compared to the physical adsorptions (Getman et al., 2012). Kosa et al. (2008) investigated the effect of Mg^{2+} and Ni^{2+} open metal sites on H_2 binding energies by applying DFT simulations. These M^{2+} sites were modeled by a neutral square pyramidal cluster, ($ML_3L'_2$, with L = CH_3OCH_3 and L′ = OCH_3^-). The H_2 binding energies are calculated as 1 kJ/mol for MOF having Mg^{2+} and 6 to 23 kJ/mol for the MOF having Ni^{2+}. The increase in the adsorption energy is attributed to the Kubas-type interaction observed in the framework having Ni^{2+}.

Sun et al. (2007) investigated H_2 interaction with Mn^{2+} sites of Mn_4Cl-MOF by applying DFT (Getman et al., 2012). They also displaced Mn by other transition metals such as Sc, Ti, V, and Cr, and evaluated H_2-MOF interactions. According to the results, H_2 binding energies for Sc-MOF, Ti-MOF, V-MOF, Cr-MOF, and Mn-MOF are calculated as 21.9 kJ/mol, 34.6

kJ/mol, 46.5 kJ/mol, 10.4 kJ/mol, and 8.4 kJ/mol, respectively. Binding energies between transition metal centers and H_2 depend on the type and group of the transition metals in the framework which at the end effects the strength of the Kubas-type interactions.

Kapelewski et al. (2018) studied H_2 storage capacity of Ni_2(m-dobdc) (m-dobdc^{4-} = 4,6-dioxido-1,3-benzenedicarboxylate) and they recorded the highest volumetric H_2 capacity in MOFs compared to the published literature so far (Lu & Ding, 2020). H_2 storage capacity of Ni_2(m-dobdc) is 11.0 g/L H_2 at 297 K and increases to 23.0 g/L as temperature decreases to 198 K at pressure range of 100-5 bar.

2.1. Studies on H_2 storage of Mixed-Metal Organic Framework

One-pot synthesis and post-synthesis modification are synthesis methods of MM-MOFs. One-pot is a direct synthesis of MM-MOFs using different kind of metals as precursors. Also, MM-MOF can be directly synthesized with linkers which provide the second metal (metalloligands). If there is a difference in reactivity of the metals, MM-MOFs can not be synthesized normally. In this case, post-synthetic modifications such as metal exchange and metal insertion are reported as appropriate methods (Masoomi et al., 2019).

Experimental and computational studies on adsorption and permeation performances of MM-MOFs have been raised significantly in the recent years. Botas et al. (2010) investigated H_2 adsorption properties of MOF-5 by partially incorporating Co^{2+} into the structure. Although, pristine MOF-5 only contains Zn atoms as metal centers and does not contain any open metal sites, inclusion of the Co^{2+} in the structure increases material's H_2 adsorption capacity at 77 K and increasing pressure up to 10 bar. Peedikakkal and Aljundi (2021) synthesized series of M-MOF-5 (M = Ni^{2+}, Co^{2+}, and Fe^{2+}) and investigated their H_2 adsorption capacities. H_2 adsorption capacities at 77 K and 1.1 bar are measured as 1.46 wt %, 1.53 wt %, 1.53 wt %, and 0.99 wt % for MOF-5, Co-MOF-5, Ni-MOF-5, and Fe-MOF-5. These two studies showed that the H_2 storage capacity of Zn-based MOF-5 can be increased by the presence of additional transition metals such as Co, Ni.

Assoualaye et al. (2020) theoretically investigated the H_2 adsorption capacities of a series of Co-doped MOF-5 materials, namely Co8-MOF-5, Co16-MOF-5, and CoMOF-5. Eight and sixteen Zn atoms are substituted by Co in Co8-MOF-5 and Co16-MOF-5, respectively. In the case of CoMOF-5, all Zn atoms of MOF-5 are substituted by Co. They

carried out GCMC simulations at 298K and 1–100 bars. The three-site Darkrim-Levesque (DL) model is applied for modeling H_2. Lennard-Jones (LJ) and Coulomb potentials are considered for modeling interactions between atom pairs. While isosteric heat of adsorption of MOF-5 is calculated as 4.91 kJ/mol, adsorption capacity of MOF-5 is determined as 1.35 wt% as gravimetric and 9.38 gH_2/L as volumetric at 100 bar. The Co-doped MOF-5 (CoMOF-5) series, on the other hand, give similar surface area (3898 m^2g^{-1}) and isosteric heat of adsorption values (4.95 kJ/mol) with pristine MOF-5 (3934 m^2g^{-1}, 4.91 kJ/mol). Co incorporating into MOF-5 structure have not been found to improve the H_2 storage characteristic of the MOF-5 adsorbent. On the other hand, results in obtaining Co8-MOF-5 and Co16-MOF-5 materials having higher density, less pore volume, less void fraction and less gravimetric surface area compared to MOF-5 and CoMOF-5. Isosteric heat of adsorption of H_2 is measured as 5.86 kJ/mol and 5.34 kJ/mol for Co8-MOF-5 and Co16-MOF-5, respectively. In addition to obtaining higher heat of adsorption with respect to MOF-5 and CoMOF-5, increase in volumetric H_2 adsorption capacities of Co8-MOF-5 (11.11 gH_2/L) and Co16-MOF-5 (10.09 gH_2/L) are reported. They observed decreased gravimetric H_2 adsorption capacities of Co8-MOF-5 (1%) Co16-MOF-5 (1.13%) which is attributed to the decreased gravimetric surface area. As a result, Co doping is shown to be a method for enhancing H_2 storage capacity of MOF-5 at ambient temperature.

Han and Goddard (2007) theoretically investigated Li-doped MOFs which include Zn_4O secondary building units and carboxylate links (Suh et al., 2012). Their GCMC simulations showed that Li doping can enhance H_2 storage at ambient conditions. H_2 uptake of Li-MOF-30 is 3.89 wt % at 20 bar, 300 K and 5.16 wt % at 100 bar, 300K. Also, H_2 uptakes of Li-MOF-30 at 100 bar are 5.57 wt % at 273K, and 5.99 wt % at 243 K. 2010 DOE target for H_2 storage is 6 wt % at 253 K to 323 K and at max 100 atm (Lochan & Head-Gordon, 2006). Thus, this study, indeed, reached the DOE target for the gravimetric H_2 adsorption.

Botas et al. (2011) synthesized MOF-74 with various Zn/Co ratios and investigated their H_2 adsorption performances. It is known that MOF-74 has open metal sites. They compared their results with the results obtained for the Co-substituted MOF-5 (Botas et al., 2010). Thus, the effects of Co^{2+} ions incorporated into Zn-based MOFs with (MOF-74) and without open metal sites (MOF-5) on H_2 adsorption have been evaluated. H_2 adsorption of MOF-5 is better than MOF-74 at 10 bar and 77 K. However, under the conditions of 1 bar and 77 K, H_2 adsorption capacity of MOF-74 increases as 36% with respect to MOF-5. As a result of this work, the H_2 adsorption capacity is related to the void space of the MOFs at high pressures and attractive interactions between the framework and H_2 at low pressures.

Kaur et al. (2016) obtained MM-MOF by partially replacing Zn^{2+} with Co^{2+} in ZIF-8, which is a zeolitic imidazolate framework and a sub-class of the MOFs. H_2 adsorption of Zn-ZIF-8 which has 0.5819 cm^3/g pore volume and 1131.1 m^2/g surface area is measured as 1.26 wt% at 77 K, 1 bar. Co doped ZIF-8, $Co_{75}Zn_{25}$-ZIF-8, which has 0.7750 cm^3/g pore volume, 1571.7 m^2/g surface area exhibits the best adsorption capacity (1.55 wt %) among the synthesized MOFs in this study. They attributed improved H_2 adsorption capacity to increment in pore volumes and coexistence of Co^{2+} and Zn^{2+} in the framework.

Dinca and Long (2007) investigated MM-MOFs versions of $Mn_3[(Mn_4Cl)_3(BTT)_8(CH_3OH)_{10}]_2$ (BTT^{3-} 1,3,5 = benzenetristetrazolate) materials. These MM-MOFs include Mn^{2+}/Li^+, Fe^{2+}, Co^{2+}, Ni^{2+}, Cu^{2+}, Zn^{2+} transition metals. H_2 storage capacities of examined materials are reported between 2.00 and 2.29% at 77 K and 1.19 bar. MM-MOF containing Co^{2+} has the highest enthalpy of adsorption (10.5 kJ/mol) among the considered materials.

Peedikakkal and Aljundi (2020) synthesized M-CuBTC (M = Ni^{2+}, Co^{2+}, Zn^{2+} and Fe^{2+}) MM-MOFs. MM-MOFs have higher gravimetric H_2 uptake compared to Cu-BTC. H_2 adsorptions of Cu-BTC, Ni-Cu-BTC, Zn-Cu-BTC, Fe-Cu-BTC, Co-Cu-BTC are 1.02, 1.61, 1.63, 1.63 and 1.12 wt%, respectively (at 77 K and 0-1.1 bars). They pointed that increasing in the binding enthalpy of H_2 due to the presence of the open metal sites can enhance the H_2 adsorption. Basic binding sites in the pores of the Cu-BTC are offered by Cu ions which have greater charge density. These metal ions result in obtaining higher binding enthalpy and H_2 is actively polarized by these open metal sites.

Villajos et al. (2015) synthesized MOF-74 materials using different Co/Ni proportions. Ni50Co-MOF-74 with a pore volume of 0.54 cm^3/g have the highest H_2 storage. The pore volume of Co-MOF-74 and Zn-MOF-74 are 0.57 cm^3/g and 045 cm^3/g, respectively. The improvement of H_2 storage is related to the presence of open metal sites as well as small pore size distribution of the material. Andrés et al (2019) synthesized Co-IRMOF-74 which has 0.86 cm^3/g pore volume and Co is partially substituted by Ni with different ratios. Topologies of these synthesized MOFs are similar to Co-MOF-74. H_2 adsorption capacity of Co-IRMOF-74 is reported as 1.16 wt % and 9.97 g/L at 298 K and 170 bar. Ni50Co-IRMOF-74 has 0.78 cm^3/g pore volume and shows the best H_2 adsorption performance with 1.24 wt % and 11.64 g/L. Isosteric heat of adsorption value of Ni50Co-IRMOF-74 is approximately 15 kJ/mol. This value is lower limit of isosteric heat of adsorption for ideal H_2 storage at ambient temperatures.

3. MATERIALS AND METHODS

In this section, Density Functional Theory (DFT) and Grand Canonical Monte Carlo (GCMC) methodologies are briefly summarized. Computational details and properties of the selected MM-MOFs are also provided.

3.1. Overview on Density Functional Theory

DFT which is developed by Hohenberg, Kohn, and Sham in 1964 is a method for minimizing ground-state energy of the systems as a function of electron density (Kohn et al., 1996). DFT is based on probability of density, p(r), instead of wavefunction, ψ. While p(r) depends on position, total energy of the system is a function of electron density. Formulation of p(r) is given in equation 3.1.1. (Atkins & De Paula, 2011).

$$p(r) = \sum_m |\psi_m(r)|^2 \quad (3.1.1.)$$

Energy terms calculated in DFT are given by equation 3.1.2.

$$E = E_{xc}[p(r)] + T_s[p(r)] + J[p(r)] + \int v_{ext}(r)p(r)dr \quad (3.1.2.)$$

$E_{xc}[p(r)]$ represents exchange and correlational energy contribution term. Exchange is essential for Pauli Exclusion Principle while correlation is essential for interaction of one electron to other electrons (Gürdal, 2017). $T_s[p(r)]$ represents the kinetic energy of the noninteracting system. $J[p(r)]$ is the coulomb potential which is arisen due to the Coulomb repulsion between electrons. $\int v_{ext}(r)p(r)dr$ is external potential. Gaussian and plane waves basis sets have been commonly used in order to calculate electron density of the system. In this thesis, these two basis sets are combined in a hybrid Gaussian and plane wave density functional. Elements of Kohn-Sham matrix is ensured using Gaussian basis sets. Calculation of Hartree and exchange-correlation energy carried out by plane wave basis set (Lippert et al., 1997).

Formulation of $E_{xc}[p(r)]$ is shown in equation 3.1.3. where nonclassical interaction between electrons are represented by $v_{ee}[p(r)]$ and kinetic energy of interacting system is represented by $T[p(r)]$ (Gurdal & Iannuzzi, 2017).

$$E_{xc}[p(r)] = (v_{ee}[p(r)] - J[p(r)]) + (T[p(r)] - T_s[p(r)]) \quad (3.1.3)$$

There is no exact analytical description of the exchange–correlation functional (Gürdal, 2017; Van Voorhis & Scuseria, 1998). Nonetheless, most physical and chemical properties can be captured by approximations. Approximations can be applied on many systems and environments that from solid state to liquid (Gürdal, 2017).

Generalized Gradient Approximation (GGA) which includes electron density and its gradient is one of the most popular methods for calculating contribution of exchange-correlation energy to the total energy (Boese et al., 2000; Gürdal, 2017). Semiempirical functionals such as Perdew-Burke-Ernzerhof (PBE) and Becke exchange/Lee-Yang-Parr correlation (BLYP) are commonly used in GGA. These semiempirical functionals have one or more parameters that are in good agreement with experimentally observed quantities (Gürdal, 2017). In this thesis, PBE density functional and DFT-D3 (Grimme D3) van der Waals dispersion interaction correction scheme have been applied in DFT calculations (Grimme et al., 2010; Perdew et al., 1996).

3.2. Basic Principles of Grand Canonical Monte Carlo Method

Identification of system is based on microscopic and macroscopic properties. Microscopic properties are used to determine thermodynamic properties of system and states of each molecule is identified by macroscopic properties. Statistical mechanics defines thermodynamic properties from the point of atomic and molecular properties. In this way, these two properties relate to each other. Classical and quantum mechanics are, in principle, able to express microscopic properties but characterization of macroscopic assembly of atoms is impractical. In this point, statistical mechanics can provide average or most possible states and relates microscopic world to the macroscopic environment (Gürdal, 2013). The probability of obtaining an i^{th} state of a system is given equation 3.2.1. where E_i is an energy and T is a temperature.

$$p_i = \frac{e^{-E_{i/K_B T}}}{\sum_{i=1}^{N} e^{-E_{i/K_B T}}} \quad (3.2.1)$$

$\sum_{i=1}^{N} e^{-E_{i/K_B T}}$ is canonical partition function (Q). Equation 3.2.2 shows that Q is defined as integration on position (r^N) and momenta (p^N) for system including N particles.

$$Q = \int dp^N \, dr^N e^{-E_{(p^N, r^N)/K_B T}} \quad (3.2.2)$$

For any property of the system, A, its ensemble average value, $\langle A \rangle$, which includes probability of occurrence can be calculated using distributions of instantaneous values of A as shown below (equation 3.2.3).

$$\langle A \rangle = \int A.p(A).dA \quad (3.2.3)$$

$\langle A \rangle$ is expressed by Q as shown in equation 3.2.4.

$$\langle A \rangle = \frac{\int dp^N dr^N A(p^N, r^N) e^{-E\left(p^N, r^N\right)_{K_B T}}}{\int dp^N dr^N e^{-E(p^N, r^N)_{K_B T}}} \quad (3.2.4)$$

Since it is impractical to calculate partition function and use equation 3.2.4 to calculate ensemble average of a property A, Monte Carlo (MC) importance sampling which was introduced by Metropolis et al. (1953) is one of the numerical methods that can calculate average of function A (Metropolis et al., 1953). Random walk of configuration of system is generated using of MC procedure and details of that procedure can be found elsewhere (Allen & Tildesley, 2017; Gürdal, 2013).

The mostly used ensembles of Monte Carlo Method are canonical, microcanonical, isobaric-isothermal, and grand canonical ensembles (Zhang et al., 2018; Frenkel, 2004). Choosing the ensemble type is based on which quantities will be kept constant during the simulations. Temperature, volume, and number of particles are kept constant in canonical ensemble. Energy, volume and number of particles are kept in constant in microcanonical ensemble. Temperature, pressure and number of particles are kept constant in isobaric-isothermal ensemble. Chemical potential, volume and temperature are kept constant in grand canonical ensemble.

In this thesis, we have applied Grand Canonical Monte Carlo (GCMC) simulations in order to predict H_2 adsorption isotherms (Basdogan & Keskin, 2015). Considering experimental aspect of the adsorption process, when the system reaches equilibrium chemical potential of the adsorbed gases and gases at the reservoir should be equal to each other (Gürdal, 2013; Zhang et al., 2018). In the GCMC simulations, average number of particles are established as a function of external conditions (e.g., temperature and pressure) (Gürdal, 2013). Temperature, volume, and chemical potential are kept constant during GCMC simulations while fluctuations of number of particles are allowed (Zhang et al., 2018) These fluctuations are generated throughout MC simulations by trial moves. Trial moves of GCMC are displacement, insertion and removal of particles (Frenkel, 2004). These trial moves refer random displacements of randomly selected particles. Firstly, a particle is randomly selected and random displacement is assigned to this particle. In condition that energy of the new configuration $U_{(n)}$ is lower than

energy of the old configuration $U_{(o)}$, new position of the atom is accepted. Acceptance rule must be considered if $U_{(n)}$ is higher compered to $U_{(o)}$. This means that new configuration is accepted by Boltzmann-type weighting principle (Frenkel, 2004; Gürdal, 2013). Equilibrium concentration of the adsorbed molecules are obtained by imposed temperature and chemical potential. Isotherms of H_2 adsorption are then determined by changing pressures (Gürdal, 2013).

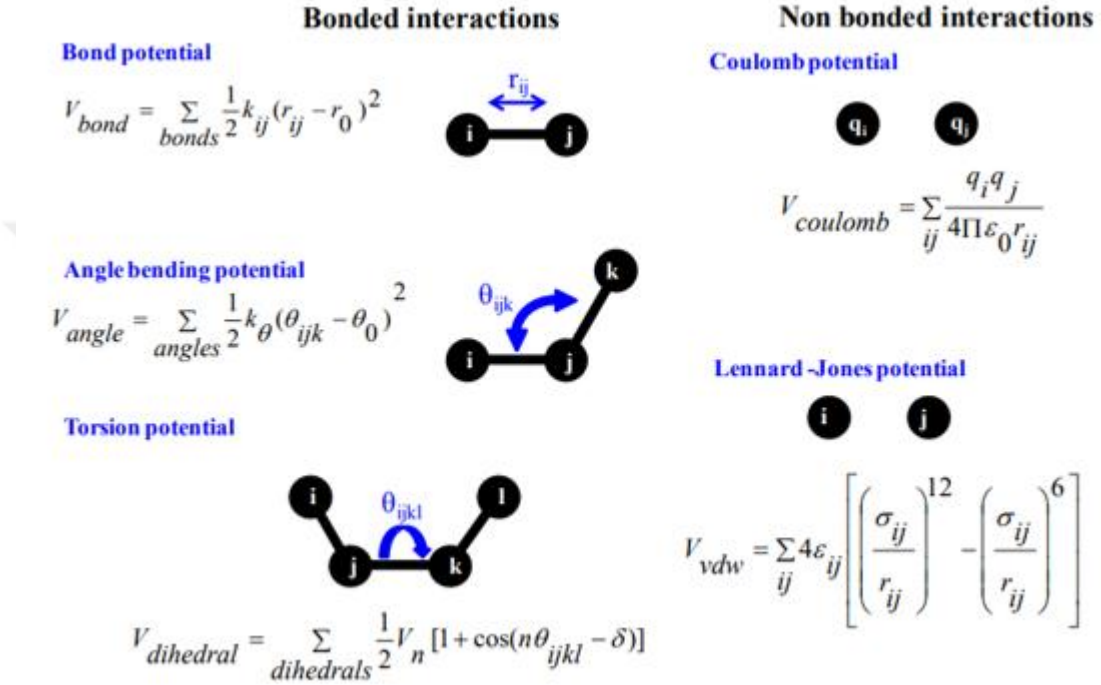

Figure 3.1. Summary of bonded and non-bonded interactions. Bonding potentials (left) represent bond, angle bending and torsion from top to bottom where k is a force constant, r_{ij} is the distance between twp particles, θ_{ijk} is the angle between three particles, θ_{ijkl} is the dihedral angle between four (i, j, k, l) particles, equilibrium bond length is represented by r_0 and equilibrium bond angle is represented by θ_0. Non-bonding (right) includes Coulomb and LJ potentials from top to bottom (Dantu, 2012).

Potential energy of a system is calculated by summing of all potentials. Typical potentials for both bonded and non-bonded interactions are summarized in Figure 3.1. Dispersion interactions are calculated by Lennard-Jones (LJ) potential and electrostatic interactions are calculated by Coulomb's potential. LJ interactions between i and j molecules are shown in Equation 3.2.6 where σ_{ij} and ε_{ij} are force fields parameters and r addresses the distance between i and j particles (equation 3.2.7).

$$V(r) = 4\varepsilon \times \left[\left(\frac{\sigma_{ij}}{r_{ij}} \right)^{12} - \left(\frac{\sigma_{ij}}{r_{ij}} \right)^{6} \right] \quad (3.2.6)$$

$$r = \sqrt{\left(x(i) - x(j)\right)^2 + \left(y(i) - y(j)\right)^2 + \left(z(i) - z(j)\right)^2} \quad (3.2.7)$$

σ_{ij} and ε_{ij} are calculated using Lorentz-Berthelot rule which is shown in Equation 3.2.8 and 3.2.9, respectively.

$$\sigma_{ij} = \frac{\sigma_{ii}+\sigma_{jj}}{2} \quad (3.2.8)$$

$$\varepsilon_{ij} = \sqrt{\varepsilon_{ii} \times \varepsilon_{jj}} \quad (3.2.9)$$

Coulomb's potential is shown in Equation 3.2.10 where q represents charges and ε_0 represents the constant of permittivity.

$$\sum_{ij} \frac{q_i q_j}{4\Pi\varepsilon_0 r_{ij}} \quad (3.2.10)$$

3.3. Belof Stern Space (BSS) Model

Using isotropic H_2 potentials is suitable for systems having dominant dispersion interactions. Buch model is isotropic H_2 potential including Lennard-Jones parameters and has been widely used in the literature. Using isotropic potentials, in fact, is not an appropriate approach for predicting H_2 adsorption with high accuracy, since electrostatic quadrupole effects which are neglected in Buch model could have an effect on predicted H_2 loadings in heterogeneous systems (Belof et al., 2008; Franz et al., 2018).

Belof-Stern-Space (BSS) is an anisotropic H_2 potential and employs five-site charge–quadrupole model for simulating H_2 in calculations benefit from classical formalism (Belof et al., 2008; Kökçam-Demir et al., 2020). The potential energy function includes electronic dispersion interactions and electrostatic interactions and is shown in equation 3.3.1.

$$U = U_{rd} + U_{es} \quad (3.3.1)$$

where U_{rd} is the energy of electronic repulsion/dispersion, U_{es} is the electrostatic energy. Parameters of BSS model are shown in Table 3.1 where q is charge, ε and σ are the Lennard-Jones force field parameters of energy and size.

Table 3.1. Parameters of the BSS model (Franz et al., 2018).

Site Name	**x (Å)**	**y (Å)**	**z (Å)**	**Mass (amu)**	**q (e)**	**ε (K)**	**σ (Å)**
H2G	0	0	0	0	-0.74640	8.8516	3.2293
H2E	-0.37100	0	0	1.00800	0.37320	0	0
H2E	0.37100	0	0	1.00800	0.37320	0	0
H2N	0.32900	0	0	0	0	4.06590	2.34060
H2N	-0.32900	0	0	0	0	4.06590	2.34060

Franz et al. (2018) carried out GCMC simulation in order to predict H_2 isotherms of Cu-TDPAH at 87 K and 77 K up to 1 atm. Cu-TDPAH which includes open metal sites consists coordination of Cu^{2+} ions and 2,5,8-tris(3,5-dicarboxyphenylamino)-1,3,4,6,7,9,9b-heptaazaphenalene (TDPAH) ligands. They compared experimental and calculated H_2 adsorptions using different potentials, such as BSS, DL, Buch, and BSSP. They used LJ potential for repulsion/dispersion interactions and electrostatic interactions are calculated by Ewald summation of the partial point charges. The Buch model underpredicts experimental H_2 isotherms. DL model overestimates experimentally measured H_2 isotherms which is attributed to the inflated electrostatic energy in simulations. Magnitude of the partial charges used in DL model (0.468 e, -0.936 e, 0.468 e) are higher than the BSS model. BSS slightly underpredicts actual H_2 loadings up to 0.6 atm at 77 K. However, predicted H_2 isotherm of the BSS is in a good agreement with experiments at higher pressures. The BSS model slightly underpredicts H_2 adsorption at 87 K and at a variety of pressure points. As a result, the more accurate predictions of the H_2 isotherms can be obtained by the BSS model compared to DL and Buch potentials.

3.4. Assigning Charges for Framework Atoms

In GCMC simulations, we consider both Lennard-Jones and electrostatic interactions into consideration. Density Derived Electrostatic and Chemical Changes (DDEC) method is applied for determining charges of the framework atoms which are needed for calculating electrostatic interactions between MOF atoms and H_2 molecules. DDEC is developed on the basis of DFT

and introduced by Manz and Sholl (2010). Net atomic charges are optimized simultaneously in this method. Chemically meaningful atomic charges are produced and electrostatic potential can be reproduced outside the electron distribution.

Applicability of the DDEC is, in principle, wide because DDEC can be used for systems which are periodic, dense solids, porous solids, surfaces of solids, small molecules, large molecules, and also materials containing buried atoms. Manz and Sholl (2010) compered the DDEC method with other charge assignment methods. According to their results, REPEAT method gives accurate results in nonperiodic systems which do not include buried atoms, however constraints are required for systems including buried atoms. The Hirshfeld (HD) method underestimates the net atomic charges. Stockholder atom (ISA) which fails system containing buried atoms and iterative Hirshfeld (IH) which overestimates charge magnitudes are not proper for the nonporous solids. The Bader method can not accurately reproduce electrostatic potential outside the electron distribution. They obtained the most accurate results applying the DDEC and there are no constraints needed in this method. The reason for obtaining more accurate charges using DDEC is attributed to the fact that DDEC ensures transferability between associated systems, specifies amount of charge transfer, reproduces electrostatic potential outside the electron distribution. Also, net atomic charges can be calculated for a variety of systems, both periodic/non periodic and with/without buried atoms.

3.5. Computational Details

The Gaussian and plane wave (GPW) formalism is used for electronic structure calculations implemented in CP2K/QUICKSTEP package (VandeVondele et al., 2005). Interactions of valence electrons and the atomic cores are expressed by Goedecker-Teter-Hutter (GTH) pseudo potentials (Goedecker et al., 1996). Basis sets which is selected as Double-zeta valence plus polarization (DZVP) optimized on molecular geometries (Mol-Opt method) are used for all kinds of atoms (VandeVondele & Hutter, 2007). PBE density functional and DFT-D3 (Grimme D3 method) van der Waals dispersion interaction correction are used in DFT calculations (Grimme et al., 2010; Perdew et al., 1996).

DFT simulations are performed in order to obtain geometry optimized structures of the MM-MOFs under consideration. By doing geometry optimization, atomic positions of the MOFs have been relaxed without topological deformation. DDEC method have been applied to the optimized MOF structures in order to determine atomic point charges with high accuracy (Manz & Sholl, 2010). DDEC code requires electron distribution cube files of the MOFs for

calculating point charges, thus single point DFT calculations have been applied to the optimized MOFs in order to obtain electron density cube files (Limas & Manz, 2018). Thus, electronic density distributions of MM-MOFs have been used as input in the DDEC code.

Following, MC simulations have been applied in grand canonical ensemble by keeping chemical potential, volume, and temperature (μVT) constant. The optimized positions of the MOF atoms have been kept fixed throughout the GCMC simulations (Düren et al., 2009; Wang et al., 2012). Raspa Code has been used to carry out GCMC simulations and obtaining GCMC snapshots of the simulated systems (Dubbeldam et al., 2016). H_2 adsorption isotherms for each MM-MOF have been calculated at 233 K and between 1-100 bar feed pressures. These temperature and range of pressures conform with DOE criteria which states that the favorable temperature should be between 233 K - 333 K and favorable pressure is between the range of 5-12 bar for H_2 Storage for light-duty vehicles.

Regarding the theoretical investigation of the H_2 adsorption performances of the MOFs, it is important that both H_2 and MOF parameters are correct and complete (Franz et al., 2018). In this thesis, H_2 is modeled by the five-site BSS model which is extensive considering the generally applied three-site model in the literature (Belof et al., 2008). The Lennard-Jones potential is used to model the dispersive interactions and the force field parameters have been taken from the Universal Force Field (UFF) (Rappé et al., 1992). Adsorption enthalpies of MM-MOFs have been extracted from the GCMC simulations. 6 MM-MOFs that display the highest H_2 storage performance have been determined for further electronic structure analysis. Electron density differences and molecular orbital distribution analysis of these selected 6 MM-MOFs have been examined by DFT in order to shed light on the reasons of the enhanced H_2 uptakes observed for these MM-MOFs with respect to the others under consideration.

3.6. Materials

This section includes topological and chemical properties of the MM-MOFs under consideration. In this thesis, we select wide variety of MM-MOFs which have different pore sizes, pore diameters, atom types and ligands in order to better identify the H_2 storage characteristics of the MM-MOFs which will be helpful for providing design strategies for future studies. We select two groups of MM-MOFs in this thesis and H_2 storage performances of the selected MM-MOFs have never been investigated so far. The first group is composed of materials which are synthesized experimentally as well as includes totally 15 MM-MOFs and

the properties of these materials are summarized in Table 3.2. You et al. (2018) studied metal substitution of M-BTCs (BTC = benzene-1,3,5-tricarbocylate) which are composed of hypothetical MOFs (Mg, Ti, V, Mn, and Co) and experimentally reported MOFs (Cr, Mo, Fe, Ru, Ni, Cu and Zn). They composed MM-BTCs by replacement of metal kinds with another metal kinds in M-BTC, in their later study (You et al., 2020). In this way, they obtained 11 MM-BTC which were also optimized. The second group of MM-MOFs is composed of 11 geometry optimized MM-BTCs which are taken from You et al. (2020) study and topological and chemical features of these 11 geometry optimized MM-BTCs are reported in Table 3.3. Their pore limiting diameter (PLD) and large cavity diameter (LCD) values are calculated in this thesis using Zeo++ software (Willems et al., 2012). Crystallographic information of the first group MM-MOFs have been obtained from the Coremof Database (*Metal Organic Framework Database | Mofs*, n.d.). Void fraction values of YEZKOF, GIFKEL and QIXSOG are calculated using RASPA package. In the literature, Li-doped MOFs have been mostly investigated for H_2 storage. Co, Zn, Cu, Fe, Ni metal ions have been also studied, however selected MM-MOFs in this thesis exhibit differences in terms of metal diversity compared to the literature.

Figure 3.2 shows all geometry optimized structures studied in this thesis. Group 1 materials are represented in Figure 3.2 (a-n). Topological structures of Group 2 materials are similar, however they have different metal sites in their paddle-wheel unit. Therefore, Cu-Mg-BTC is shown as an example of the structure of the Group 2 materials in Figure 3.2 (o).

Table 3.2. 1st group of MM-MOFs investigated in this thesis. Void fractions, pore limiting diameters (PLD), the largest cavity diameters (LCD) and atoms in the structures are reported (*Metal Organic Framework Database | Mofs*, n.d.).

Name	Void Fraction	PLD	LCD	Atoms in MOF
FOKGET	0.26	2.78	4.20	C, Co, N, O, W
XUWTAK	0.39	3.75	4.41	Ga, Mn, P, O
ZALDUO	0.33	3.57	4.62	N, C, W, Ni
RUCGOM	0.31	3.82	4.4	Zn, H, Pt, Au, C, S, N, O
WAVWEW	0.28	3.19	3.41	Ba, Co, H, C, O
HEFVAR	0.15	3.78	4.23	Cu, H, Rh, C, N, Cl, O
YOZJEE	0.42	3.6	4.63	N, C, H, Ag, Fe
UKULOB01	0.1	3.22	3.83	Fe, Ag, H, C, N
YOMVIG	0.5	3.38	5.31	Al, Co, P, O
XILDUT	0.41	3.97	5.33	Na, Zn, H, C, Cl, O
KALQEV	0.34	4.72	5.83	Mn, Cr, C, O
OSOYUR	0.57	5.24	5.9	Ca, Zn, H, C, O
QIXSOG	0.68	5.04	7.52	Mn, Cu, C, N
YEZKOF	0.31	3.29	6.11	Co, Mo, H, C, N, O
GIFKEL	0.41	4.32	4.63	N, C, H, Cd, Ni

Table 3.3. 2nd group of 11 MM-BTCs investigated in this thesis. Void fractions, PLD, LCD and atoms in the structures are reported (You et al., 2020). Co-Mg-BTC material is created by us in order to examine the effect of the presence of the Co on H_2 loading.

Name	Void Fraction	PLD	LCD	Atoms in MOF
Cr-Cu-BTC	0.73	6.82	12.13	H, C, O, Cr, Cu
Cr-Fe-BTC	0.74	6.89	12.20	H, C, O, Cr, Fe
Cr-Mg-BTC	0.74	6.86	12.23	H, C, O, Cr, Mg
Cr-Mn-BTC	0.74	6.96	12.21	H, C, O, Cr, Mn
Cr-Mo-BTC	0.74	7.04	12.42	H, C, O, Cr, Mo
Cr-Ru-BTC	0.74	6.95	12.61	H, C, O, Cr, Ru
Cr-Zn-BTC	0.74	6.89	12.36	H, C, O, Cr, Zn
Cu-Mg-BTC	0.74	6.78	12.51	H, C, O, Cu, Mg
Cu-Zn-BTC	0.74	6.73	13.30	H, C, O, Cu, Zn
Fe-Mg-BTC	0.74	6.85	12.10	H, C, O, Fe, Mg
Ti-Mo-BTC	0.74	7.05	12.48	H, C, O, Ti, Mo
Co-Mg-BTC	0.74	6.84	12.47	H, C, O, Co, Mg

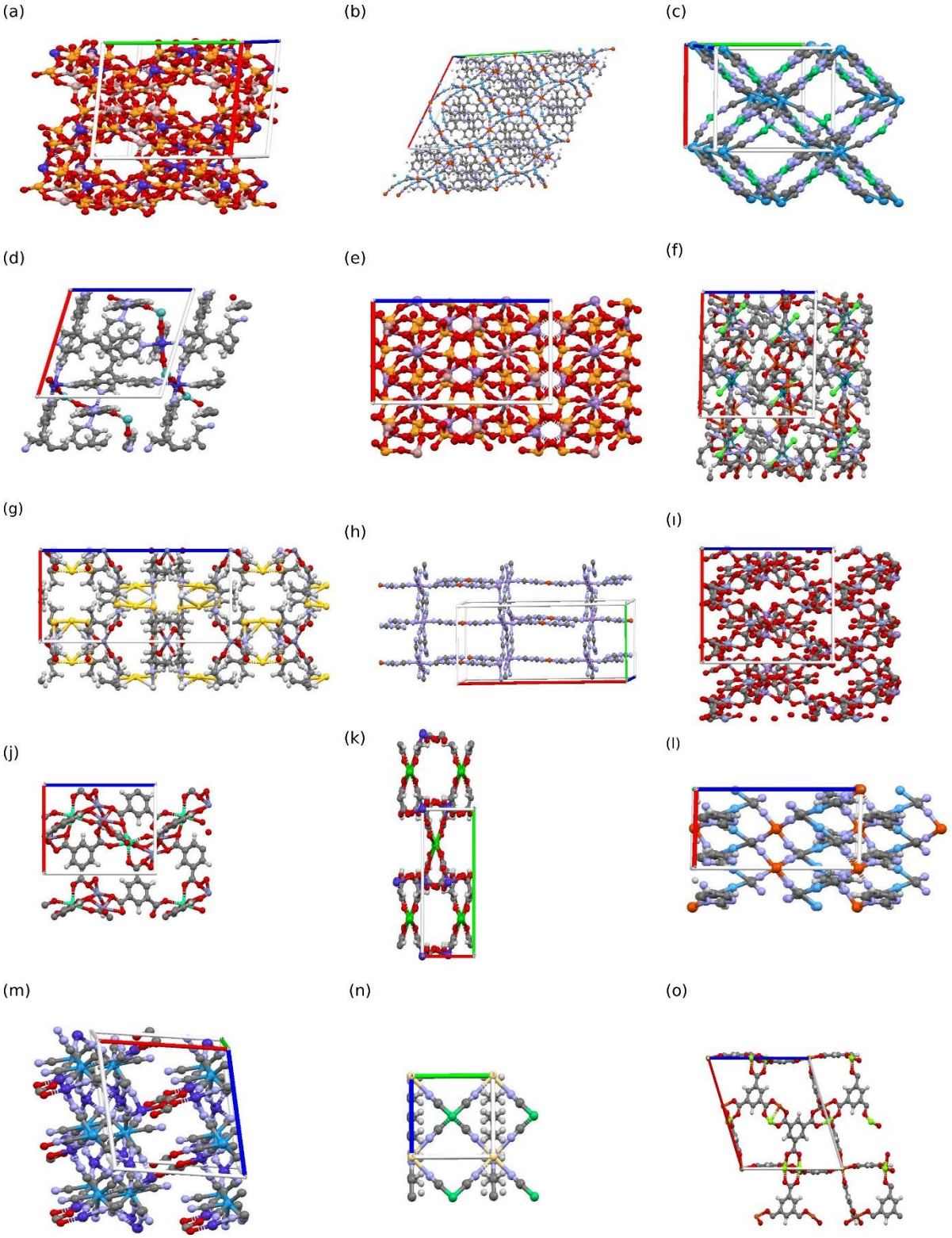

Figure 3.2. Ball and stick representations of (a) YOMVIG (b) YOZJEE (c) ZALDUO (d) YEZKOF (e) XUWTAK (f) HEFVAR (g) RUCGOM (h) QIXSOG (i) KALQEV (j) OSOYUR (k) WAVWEW (n) GIFKEL (m) FOKGET (n) UKULOB01 and (o) Cu-Mg-BTC which are modeled in this thesis.

4. RESULTS AND DISCUSSIONS

This chapter gives all results and discussions of employed simulations. Firstly, predicted H_2 adsorption isotherms of the BSS model are compared with experimental measurements. Then, correlation between H_2 storage performances of MM-MOFs and their topological/chemical features have been discussed. H_2 adsorption performances of MM-MOFs have been examined and the best H_2 adsorbing MM-MOFs have been determined. Three top-performing MM-MOFs are selected from both 1st group and 2nd group materials. Subsequently, quantum-mechanical calculations have been carried out in order to further characterize the top-performing MM-MOFs.

4.1. Modeling MOFs for H_2 Adsorption

Firstly, results of the GCMC simulations are compared with the available experimental data obtained for the H_2 loading in widely studied MOFs. Electron density cube files of IRMOF-1 and CuBTC (Copper benzene-1,3,5-tricarboxylate) have been obtained and point charges have been calculated applying the DDEC method. Void fractions of selected MOFs have been calculated using RASPA simulation package and corresponding experimental data has been taken from the NIST database (*NIST/ARPA-E Database of Novel and Emerging Adsorbent Materials*, n.d.)

Crystallographic information of the IRMOF-1 is obtained from RASPA code. The gravimetric H_2 adsorption isotherms of IRMOF-1 up to 100 bar at 298 K obtained by both experiments and the applied BSS model are shown Figure 4.1. Results suggest that calculated H_2 isotherm of IRMOF-1 is in good agreement with the available experimental data (Kaye et al., 2007). The predictions coincide well with the adsorption measurements especially up to 50 bar. Increasing feed pressure to 100 bar results in only slight deviations between the theory and the experiments.

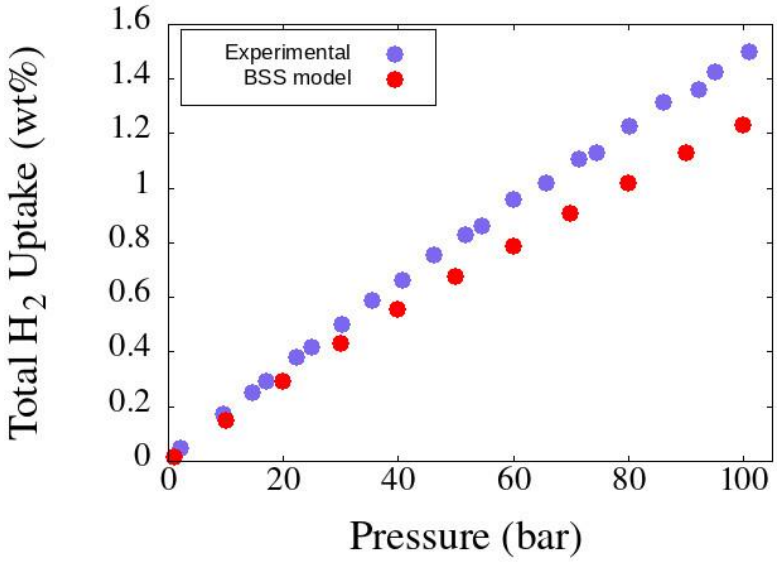

Figure 4.1. Comparison of the gravimetric H_2 adsorption isotherms of the IRMOF-1 up to 100 bar at 298 K obtained by both experiments and the applied BSS model. Red: Simulation results, purple: experimental data from Kaye et al. (2007).

Generally, H_2 adsorption isotherms have been reported in terms of excess adsorption in experimental studies. Experimental data of H_2 adsorption isotherms at 1 bar and 77 K are reported in Table 4.1 measured for IRMOF-1. Numerical values reported in the table are taken from the literature (Durette et al., 2016; Li et al., 2009; Peedikakkal & Aljundi, 2021). Excess H_2 adsorption loading is calculated as 1.1 wt% in our simulations carried out at the same temperature and pressure as the experiments, i.e. 77 K and 1 bar. As results suggest, we capture gravimetric H_2 loadings determined by the experiments.

Table 4.1 Experimental data of the gravimetric H_2 adsorption measured at 1 bar and 77 K for IRMOF-1. The results of our calculations are also reported.

H_2 adsorption (wt %)	**REFERENCE**
1.32	(Rowsell et al., 2004)
1.2	(Yang et al., 2012)
1.2	(Hirscher & Panella, 2007)
1.1	(Wong-Foy et al., 2006)
1.1	In this thesis

As a final validation test, we have compared our simulations with the experimental data carried out for the Cu-BTC. Crystallographic information of the Cu-BTC have been taken from the study of You et al. (2018). Experimental results of the gravimetric excess H_2 adsorption

isotherms of the Cu-BTC up to 100 bar and at 298 K which are taken from two different experimental study have been compared with our simulations applying the BSS model (Li & Yang, 2008; Panella et al., 2006). As it is depicted in Figure 4.2, experimental data and simulation results are in good agreement, though moderate deviations between the isotherms are also observed. We model materials as perfect crystals in our calculations, however vacancies and grain boundaries can be also observed in MOFs which are synthesis-dependent and might lead to larger adsorption of gas species. Considering this difference between experiments and simulations, discrepancies between the results are expected. As a result of the comparison study, the BSS model shows good agreement with the experimental data. Thus, we confirm that applied methodology for determining H_2 loadings is, indeed, reliable.

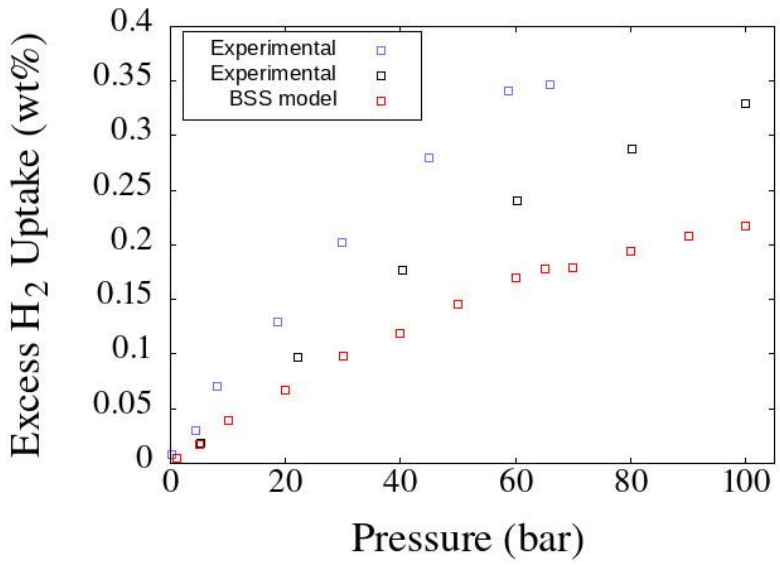

Figure 4.2. Comparison of the gravimetric H_2 adsorption isotherms of the Cu-BTC up to 100 bar at 298 K obtained by experiments and our simulations. Red: Simulation results, purple: experimental data from Panella et al. (2006), black: experimental data from Li & Yang (2008).

4.2. Adsorption of Molecular Hydrogen

In this section the results of GCMC simulations are discussed. The calculations are carried out at 233 K and between 0.1 and 100 bar feed pressure. Gravimetric and volumetric H_2 isotherms as well as enthalpies of adsorption of materials under consideration have been provided.

The gravimetric and volumetric H_2 isotherms of the 1st group materials are shown in Figure 4.3 and Figure 4.4, respectively. As a first observation, QIXSOG is the material that shows the largest gravimetric H_2 adsorption, especially at higher pressures. Among the 1st group materials, YOMVIG, QIXSOG and OSOYUR are detected as the top-performing MM-MOFs at 233 K and 100 bar. Their structure is provided in Figure 3.2 (a, h, j) in Materials and Methods section.

H_2 adsorption of QIXSOG which shows the largest gravimetric H_2 adsorption as 1.53 wt% has the highest void fraction (0.68) and LCD (7.52 Å) value among the 1st group materials. The volumetric H_2 adsorption value of QIXSOG is determined as 9.47 g/L at 100 bar. YOMVIG shows the greatest volumetric capacity among 1st group materials which is calculated as 11.33 g/L. Gravimetric H_2 storage of the YOMVIG is calculated as 0.58 wt% 100 bar. 2020 DOE target is defined as 4.5 wt % and 30 g/L H_2 capacity. However, obtaining maximization of both gravimetric and volumetric capacity is difficult (Kapelewski et al., 2018). Gravimetric and volumetric H_2 adsorption of OSOYUR are determined as 0.82 wt% and 10.89 g/L at 100 bar.

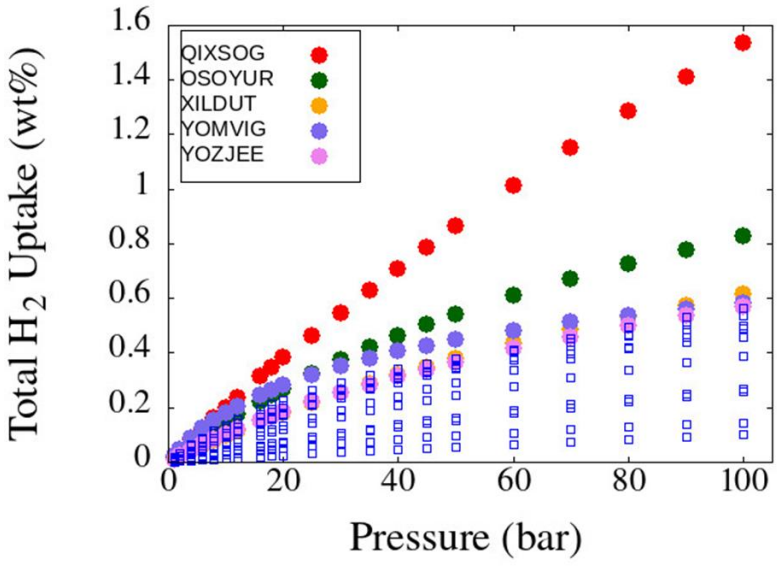

Figure 4.3. The gravimetric H_2 adsorption isotherms of the 1st group materials at 233 K. The materials showing large loadings are indicated by colorful closed cycles. The rest of the materials are shown using open blue squares.

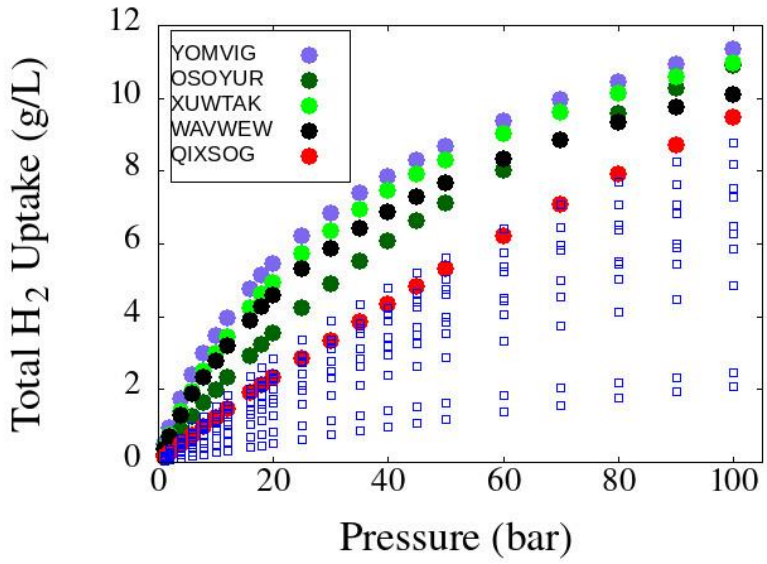

Figure 4.4. The volumetric H_2 isotherms of the 1st group materials at 233 K. The materials showing large loadings are indicated by colorful closed cycles. The rest of the materials are shown using open blue squares.

UKULOB01 shows the lowest gravimetric (0.09 wt%) and volumetric (2.09 g/L) H_2 adsorption isotherms at 100 bar. UKULOB01 and YOZJEE consist of same kinds of atoms, though YOZJEE shows relatively large gravimetric H_2 adsorption. Gravimetric and volumetric H_2 adsorption loading of YOZJEE are calculated as 0.56 wt% and 8.76 g/L, respectively at 100 bar. The structures of UKULOB01 and YOZJEE are shown in detail in Figure 4.5. Although, these two materials have same kinds of atoms, their ligand structures are different which leads to obtain different topologies for these two materials. While YOZJEE has TPT [TPT = 2,4,6-tris(4-pyridyl)-1,3,5-triazine] ligands, UKULOB01 has pmd (pmd = pyrimidine) ligands in its structure and both of them have $[M(CN)_2]^-$ (M = Ag) groups. Differences between their ligand structures results in topological differences between the materials. For instance, void fraction, PLD, and LCD of YOZJEE (0.42, 3.6 Å and 4.63 Å, respectively) are larger than UKULOB01 (0.1, 3.22 Å, and 3.83 Å, respectively).

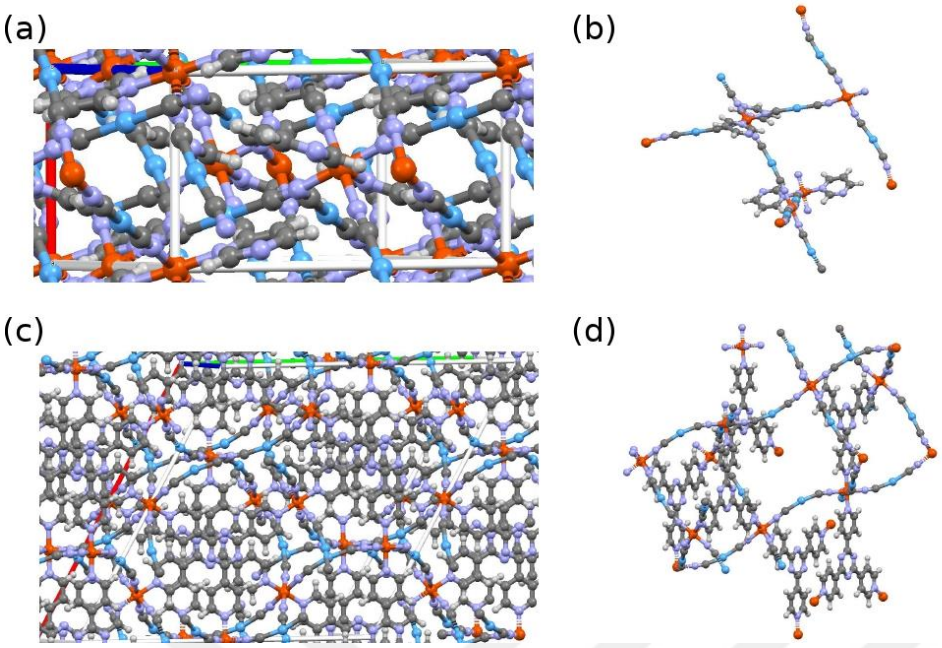

Figure 4.5. Structures of (a) UKULOB01 (b) UKULOB01 unicell (c) YOZJEE (d) YOZJEE unicell. Fe, Ag, H, C, and N atoms are represented by orange, blue, white, gray, and light blue-magenta respectively.

As a summary, materials listed under the 1st group shows promising H_2 adsorption capacities. While QIXSOG and OSOYUR show the largest gravimetric H_2 adsorption, YOMVIG, OSOYUR, XUWTAK, WAVWEW, and QIXSOG possess largest volumetric adsorption among the considered materials. While the largest gravimetric adsorption observed is 1.53 wt%, the largest volumetric adsorption becomes 11.33 g/L. Results suggest that QIXSOG, YOMVIG, and OSOYUR maximize volumetric and gravimetric H_2 adsorptions, thus they can be promising candidates to be used in H_2 storage systems. As it can be also in Table 3.2, YOMVIG has Co and Al metal nodes, QIXSOG has Mn metal node and Cu metal nodes and OSOYUR has Ca and Zn metal nodes.

The gravimetric and volumetric H_2 isotherms of the 2nd group materials re shown in Figure 4.6 and Figure 4.7, respectively. Generally, 2nd group shows higher H_2 uptake both gravimetrically and volumetrically with respect to the 1st group materials. According to the results, Cr-Mg-BTC (1.64 wt% and 12.24 g/L), Fe-Mg-BTC (1.61 wt % and 12.13 g/L) and Cu-Mg-BTC (1.56 wt % and 12.27 g/L) are observed as top-performing MM-BTCs. Their metal nodes are placed in paddle-wheel unit of the structure and they have carbon rings. PLD, LCD and void fraction values of the 2nd group are close to each other and their topological structures are also nearly same. Unlike the 1st group, the volumetric and gravimetric H_2 uptake of the 2nd group is materials are calculated to be very similar to each other.

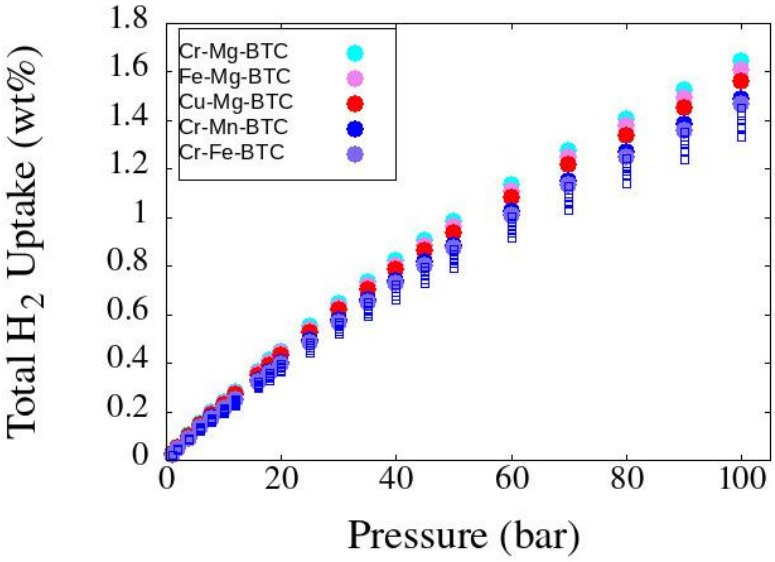

Figure 4.6. The gravimetric H_2 isotherms of the 2nd group materials calculated at 233 K. While top performing ones are shown with colorful closed cycles, the rest of the materials are depicted with open blue squares.

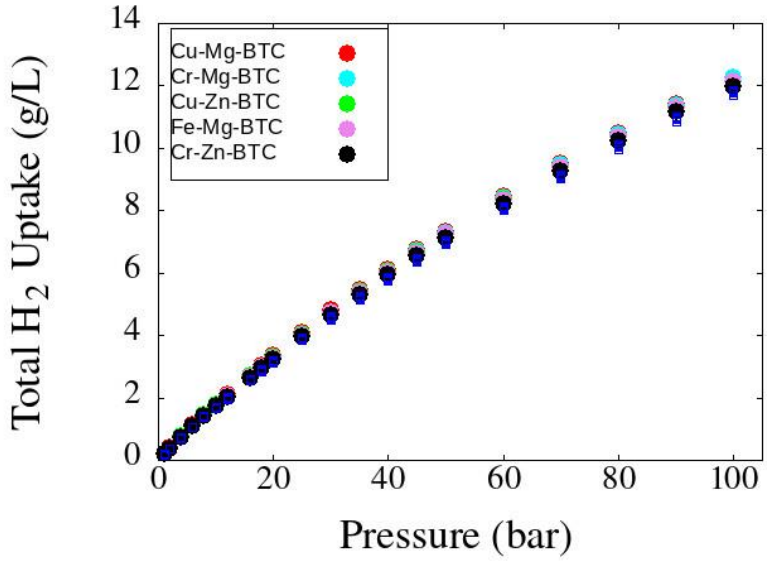

Figure 4.7. The volumetric H_2 isotherms of the 2nd group materials calculated at 233 K.

All top-performing MM-BTCs belongs to 2nd group include Mg atom. Presence of Mg atom may have affected H_2 adsorption positively. It is well known that the presence of Co metal also increases adsorption of H_2 (Peedikakkal & Aljundi, 2020). Therefore, Cr atoms of the Cr-Mg-BTC are replaced with Co atom and H_2 adsorption of the newly created Co-Mg-BTC has been investigated in this thesis. Geometry of the Co-Mg-BTC is optimized applying DFT and DDEC calculations have been carried out for the Co-Mg-BTC in order to determine partial atomic charges of the MOF atoms. Gravimetric (1.58 wt %) and volumetric (12.01 g/L) H_2

adsorption isotherms calculated for the Co-Mg-BTC are close to top-performing MM-BTCs and are shown in Figure 4.8.

As a general observation for the 2nd group materials, the Cr-Ru-BTC shows the lowest gravimetric H_2 adsorption isotherm at 100 bar which is calculated as 1.33 wt%. The Cr-Mo-BTC shows the lowest volumetric H_2 adsorption isotherm calculated as 11.71 g/L at 100 bar. However, as pointed out before, gravimetric and volumetric adsorptions of H_2 are very similar for the 2nd group materials which suggests that the topology of the frameworks as well as presence of the open metal sites affect H_2 adsorption more than the type of the transition metal in the structure.

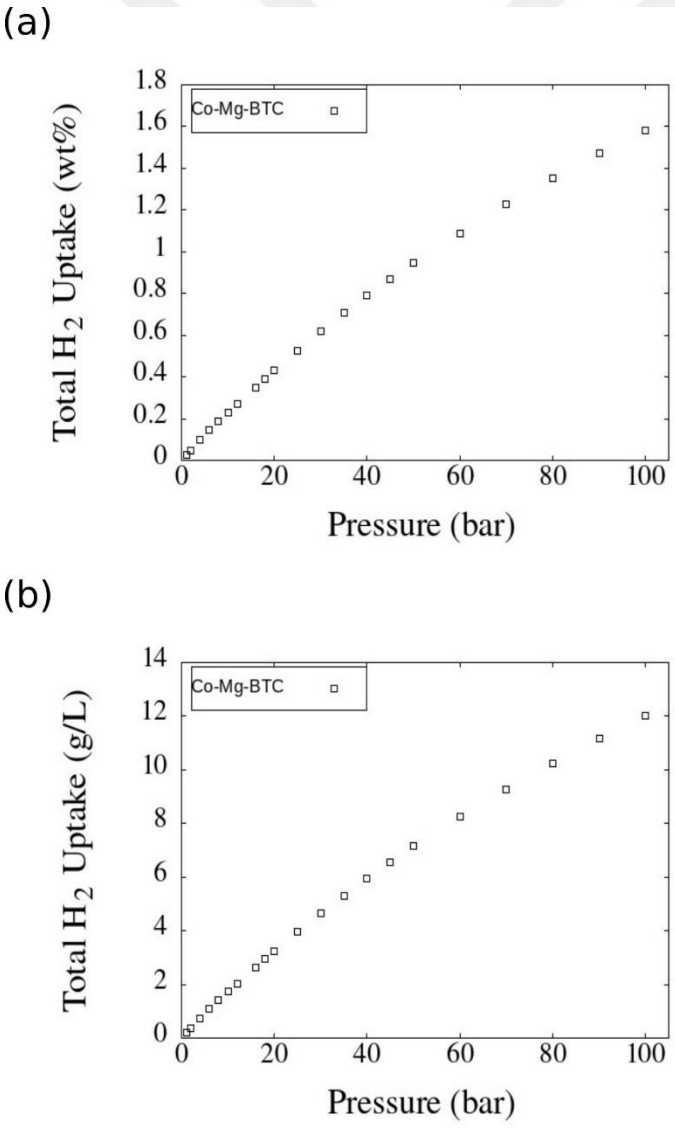

Figure 4.8. Gravimetric and volumetric H_2 isotherms of the Co-Mg-BTC calculated at 233 K.

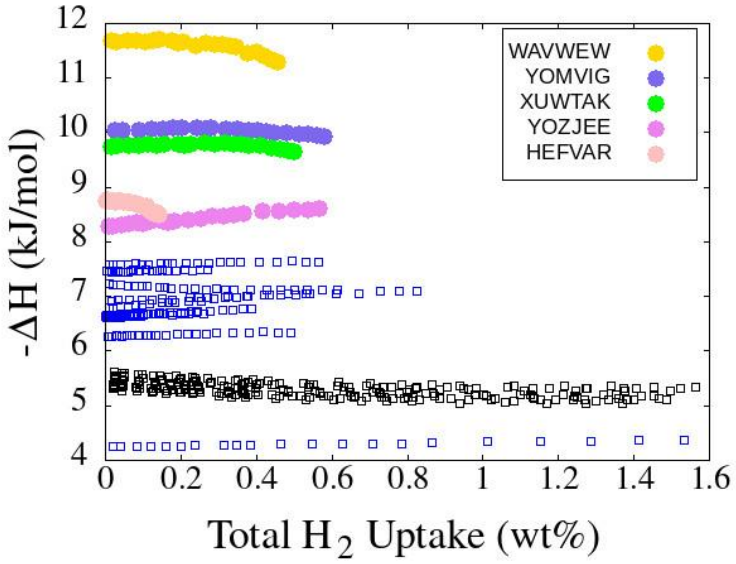

Figure 4.9. Enthalpies of adsorption of all MM-MOFs investigated in this thesis. While the materials belonging to the 1st group materials and showing large enthalpies are indicated with colorful cycles, the rest of the 1st group materials are depicted with open blue squares. All the materials belonging to the 2nd group are depicted with open black squares.

Enthalpies of adsorption of all MM-MOFs are shown in Figure 4.9. Generally, there is an opposite relationship between pore volume and isosteric heat of adsorption. H_2 can interact stronger with materials which have smaller pore size and high curvature walls. In this way, higher isosteric heat of adsorption can be obtained by smaller pore size and high curvature walls (Assoualaye & Djongyang, 2021). The strongest interaction between the H_2 and the MM-MOF is detected in WAVWEW which consists of Ba and Co metal sites in its structure. Besides, WAVWEW having the smallest LCD as 3.41 Å shows the highest enthalpy of adsorption calculated as 11 kJ/mol. Also, volumetric H_2 adsorption isotherm of the WAVWEW which is 10.09 g/L is rather high comparing with the values for the other MOFs reported in the literature. QIXSOG which belongs to the 1st group materials and possesses the highest void fraction as 0.68 as well as LCD as 7.52 Å shows the lowest adsorption enthalpy as approximately 4 kJ/mol. The topology of the QIXSOG is not suitable for a strong interaction with H_2 although it has large gravimetric adsorption as 1.53 wt%. Weak interaction depends not only on the void fraction and LCD values, but also on the ligand structure. QIXSOG have bridged dca [dca = $N(CN)_2$] ligands which are chain-like. Although topologies of the YOZJEE and UKULOB01 are similar and they include the same kind of atoms in their structures, see Figure 4.5, enthalpies of adsorption calculated for the YOZJEE and UKULOB01 are around 8 kJ/mol and 6 kJ/mol, respectively. YOZJEE has larger void fraction, PLD and LCD values as 0.42, 3.6 Å, and 4.63 Å, respectively than UKULOB01 which has corresponding values as 0.1, 3.22 Å, and 3.83 Å,

respectively. Structure of organic linkers of the YOZJEE leads to increment in heat of adsorption (Han et al., 2007). Also, strong interactions between H_2 and YOMVIG having relatively narrow LCD as 5.31 Å are deduced from the calculated enthalpy of adsorption which is high as 10 kJ/mol.

The LCD values of the 2nd group are almost twice of the 1st group materials. Enthalpies of the 2nd group materials are calculated very similar to each other which is around 5 kJ/mol. Assoualaye and Djongyang (2021) attributed high volumetric H_2 storage capacity of the nanoporous materials to isosteric heat of adsorption. From our results it can be concluded that MOFs having small LCD values have large volumetric H_2 adsorption capacity as well as large isosteric heats of adsorption. Also, atomic structures of the MOFs play a role in attracting H_2 molecules.

The binding between H_2 and metals in MM-MOFs observed at 233 K and at 100 bar are depicted in Figure 4.10 and reported in Table 4.2. We analyze only top performing MM-MOFs from the 1st and 2nd group materials which are YOMVIG, QIXSOG, OSOYUR, Cu-Mg-BTC, Fe-Mg-BTC, and Cr-Mg-BTC. Following the GCMC simulations, we have selected GCMC snapshots of the best performing MM-MOFs and we have applied geometry optimization simulations to the selected snapshots using DFT in order to accurately locate the adsorption sites of the H_2 molecules. The distances between H_2 and metal sites in top performing MM-MOFs are range from 2-4 Å to 4.44 Å, see Table 4.2. H_2 molecules are adsorbed in close vicinity of the metal sites, especially for the MM-BTCs, i.e. the 2nd group materials. The measured distance between hydrogen pairs and Mg and Cr atoms are measured approximately as 2.2 Å in Cr-Mg-BTC. The measured distances are short and similar to each other for Cu, Fe, and Cr included BTCs. For the 1st group materials, we observe slightly larger H_2-metal site distances. Electronic structure analysis of the selected MM-MOFs are provided in the next subsection.

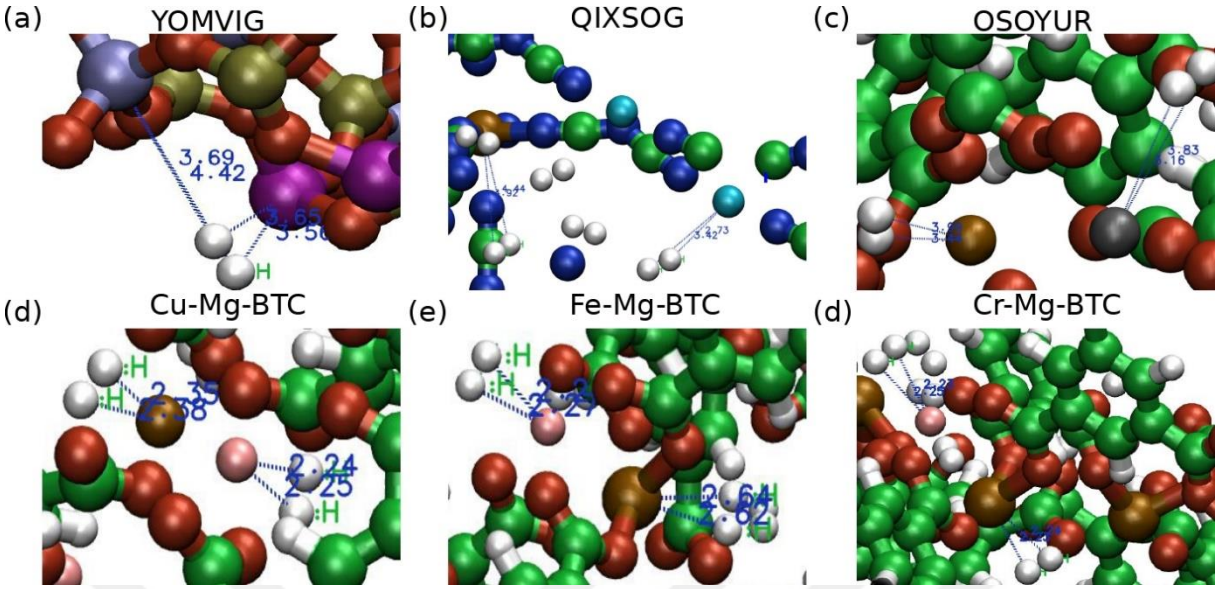

Figure 4.10. H_2 adsorption sites of (a) YOMVIG (b) QIXSOG (c) OSOYUR (d) Cu-Mg-BTC (e) Fe-Mg-BTC (f) Cr-Mg-BTC. (Al: Ice blue, Co: Purple, P: Tan, O: Red, H: White, Cu: Cyan, N: dark blue, C: Green, Zn: Gray. Mn, Cu, Fe and Cr are represented by ochre in (d), (e), and (f), respectively.

Table 4.2. Measured distances between metal sites and H_2 molecules which are provided in Å. Geometry optimizations are carried out for the selected GCMC snapshots.

MM-MOF	Metal – H distances
YOMVIG	Co – 3.56 Al – 3.66
QIXSOG	Cu – 2.73 Mn – 4.44
OSOYUR	Ca – 3.44 Zn – 3.16
Cu-Mg-BTC	Mg – 2.24 Cu – 2.35
Fe-Mg-BTC	Mg – 2.26 Fe – 2.62
Cr-Mg-BTC	Mg – 2.23 Cr – 2.23

QIXSOG have bridged dca ligands and open Cr metal sites (Kushch et al., 2007). YOMVIG is aluminophosphate molecular sieves which is composed of AlO_4 and PO_4 tetrahedra having Co and Al open metal sites (Song et al., 2009). OSOYOR has BTC ligands and open Zn metal sites (Zou et al., 2010). Cu-Mg-BTC, Fe-Mg-BTC and Cr-Mg-BTC has BTC ligands and open metals sites. Results suggets that BTC ligands are favorable for gravimetric and volumetric H_2 adsorption. Cr, Al, Co, Zn, Cu, Fe, and Mg metals are promising

open metal sites for H_2 adsorption. Properties, H_2 uptakes, as well as adsorption enthalpies of the top performing MM-MOFs are summarized in Table 4.3.

Table 4.3. Top performing MM-MOFs from the 1st and 2nd group materials investigated in this thesis. Void fraction, PLD, LCD and metal sites of the MM-MOFs are reported. Gravimetric (wt %) and volumetric (g/L) H_2 uptake and enthalpies of adsorptions are calculated at 233 K and 100 bar.

MM-MOF	Void Fraction	PLD	LCD	Metal sites	Wt %	g/L	Enthalpy of adsorption (kJ/mol)
YOMVIG	0.5	3.38	5.31	Al, Co	0.58	11.33	9.93
QIXSOG	0.68	5.04	7.52	Cu, Mn	1.53	9.47	4.37
OSOYUR	0.57	5.24	5.9	Ca, Zn	0.82	10.89	7.10
Cu-Mg-BTC	0.74	6.78	12.51	Mg, Cu	1.56	12.27	5.35
Fe-Mg-BTC	0.74	6.85	12.10	Mg, Fe	1.61	12.13	5.27
Cr-Mg-BTC	0.74	6.86	12.23	Mg, Cr	1.64	12.24	5.31

4.3. The Electron Density Difference Maps

The total density of the H_2 adsorbed MOFs, $p_{allsystem}(r)$, is subtracted from the individual electron densities of the MM-MOFs, $p_{MOF}(r)$, and H_2 molecules, $p_{molecule}(r)$, at the same atomic coordinates. In this way, the electron density differences, $\Delta p(r)$, are calculated usign the following formulation (Koizumi et al., 2019).

$$\Delta p(r) = p_{allsystem}(r) - (p_{MOF}(r) + p_{molecule}(r)) \quad (4.3.1)$$

The electronic density difference, $\Delta p(r)$, calculated for the YOMVIG is shown in Figure 4.11. Electron depletion region occurs on H_2 molecules and no electron accumulation region is observed on any hydrogen pairs. If depletion region was also observed in opposite sides of the hydrogen pairs it would be a signature of a polarization effect (Koizumi et al., 2019). Charge depletes and accumulates both on Co atoms. We have not observed charge depletion/accumulation on Al. O which located between Co and P atoms have both accumulation and depletion regions.

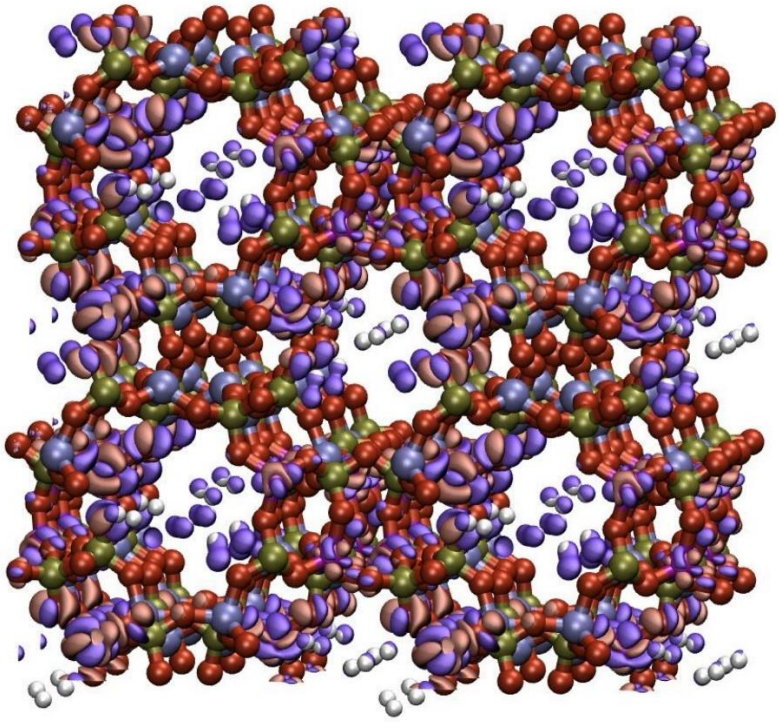

Figure 4.11. Electron density difference calculated for the YOMVIG. Isosurfaces taken at + 0.000964 e $Å^{-3}$ for charge accumulation which is represented by pink and -0.000964 e $Å^{-3}$ for charge depletion which is represented by purple. Co, P, Al and O are represented by purple, tan, ice blue, and red, respectively.

The Δp(r) for the QIXSOG is depicted Figure 4.12. Charge depletion and accumulation regions occur around Mn atoms. Only charge depletion region occurs on H_2 molecules. There is no polarization due to low dispersion interaction between QIXSOG and H_2. It is expected since QIXSOG possesses low enthalpy of adsorption value. Also, accumulation and depletion regions are observed around C and N atoms in the ligands.

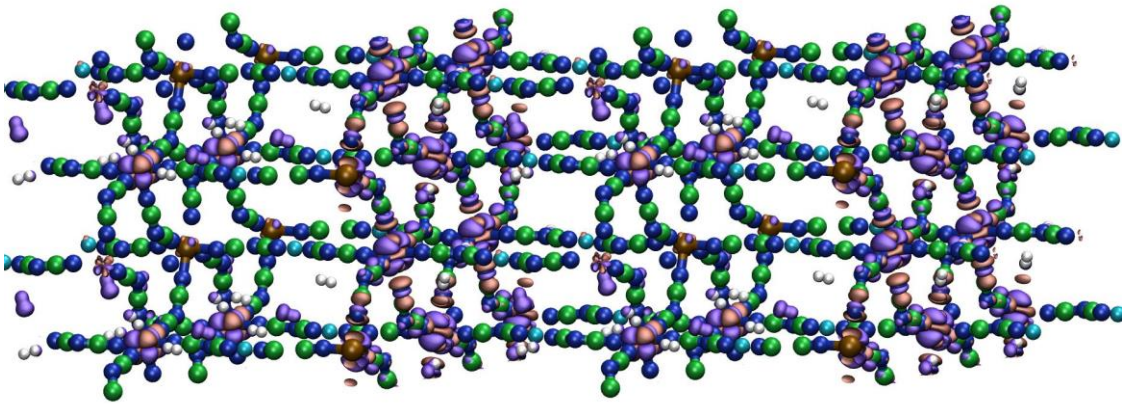

Figure 4.12. Electron density difference calculated for the QIXSOG. Isosurfaces taken at + 0.00122 e $Å^{-3}$ for charge accumulation which is represented by pink and - 0.00122 e $Å^{-3}$ for charge depletion which is represented by purple. Cu, Mn, N and C are represented by cyan, ochre, dark blue, and green, respectively.

The Δp(r) for the OSOYUR is shown in Figure 4.13. Electron depletion is observed on H_2 molecules and electron accumulation is observed in the close vicinity of these H_2 molecules. Furthermore, uneven distribution of positive charges is also observed on H_2 molecules. This situation is a sign of polarization. Polarization of H_2 pairs adsorbed on the OSOYUR is shown in detail in Figure 4.13 (b). Both charge depletion and accumulation regions occur around O atoms and slightly on Zn atoms in the structure of the MM-MOFs.

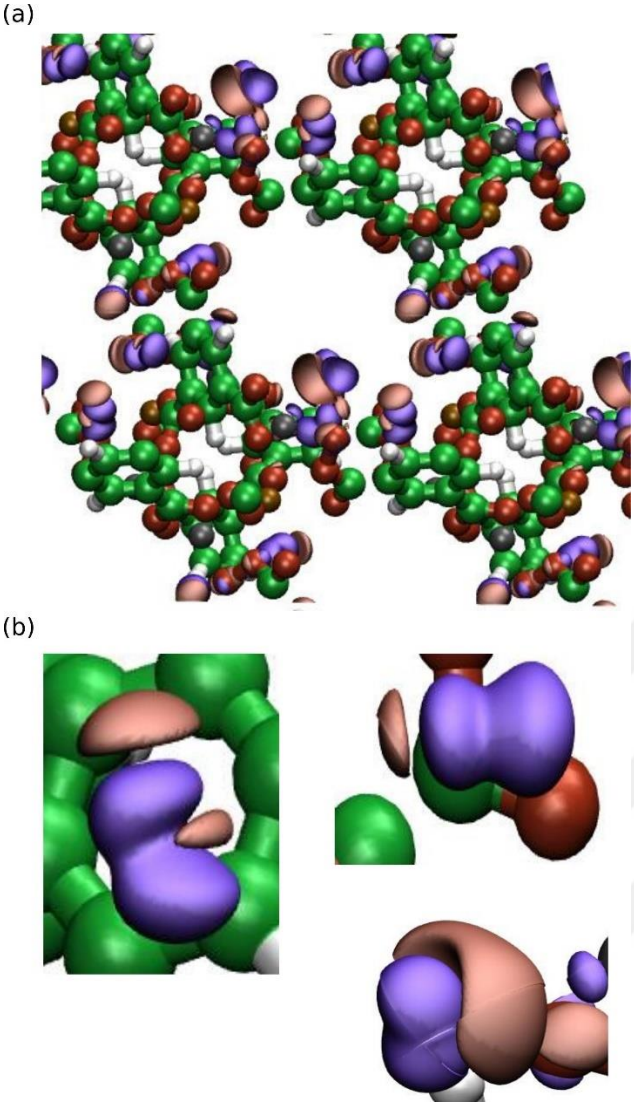

Figure 4.13. (a) Electron density difference calculated for the OSOYUR. Isosurfaces taken at +0.00035 e $Å^{-3}$ for charge accumulation which is represented by pink and - 0.00035 e $Å^{-3}$ for charge depletion which is represented by purple (b) polarizations of H_2 molecules. Ca, Zn, H, C and O are represented by ochre, gray, white, green and red, respectively.

The electron density difference calculated for the Cr-Mg-BTC is shown in Figure 4.14. Electron accumulation and uneven depletion regions occur on H_2 molecules which are located close to Mg atoms. This polarization is shown in detail in Figure 4.14 (b).

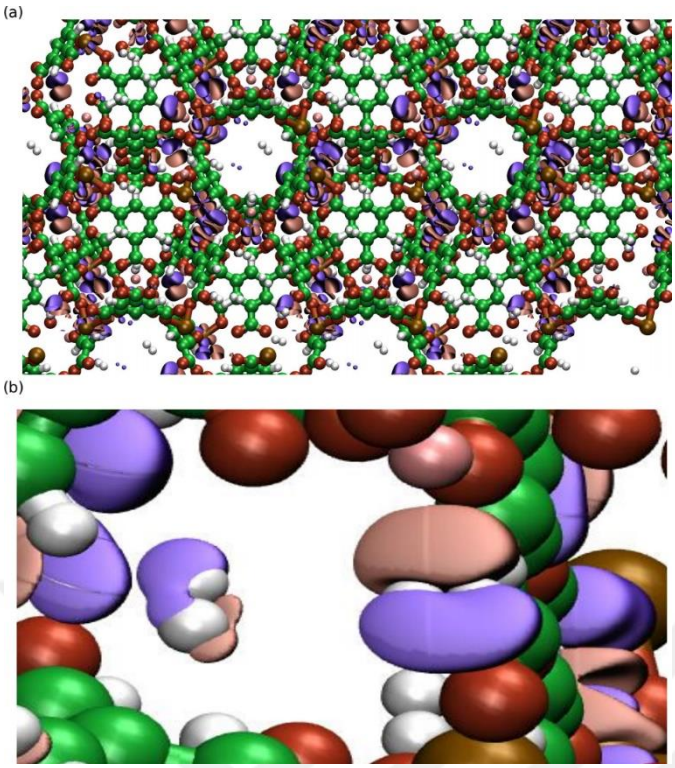

Figure 4.14. (a) Electron density difference calculated for the Cr-Mg-BTC. Isosurfaces taken at + 0.001235 e $Å^{-3}$ for charge accumulation which is represented by pink and -0.001235 e $Å^{-3}$ for charge depletion which is represented by purple (b) polarizations of the H_2 molecules. Cr, Mg, H, O and C are represented by ochre, pink, white, red, and green, respectively.

The Δp(r) for the Fe-Mg-BTC is depicted in Figure 4.15. Electron accumulation/depletion distributions of the H_2 molecules close to the Mg atoms of the Fe-Mg-BTC are similar to the H_2 molecules located close vicinity of the Mg atoms of the Cr-Mg-BTC. Some H_2 molecules have only uneven depletion regions. Electron accumulation and depletion regions occur oppositely at the ends of the H_2 molecules. Polarizations are depicted in detail in Figure 4.15 (b). Accumulation and depletion regions are observed around Fe atoms as well.

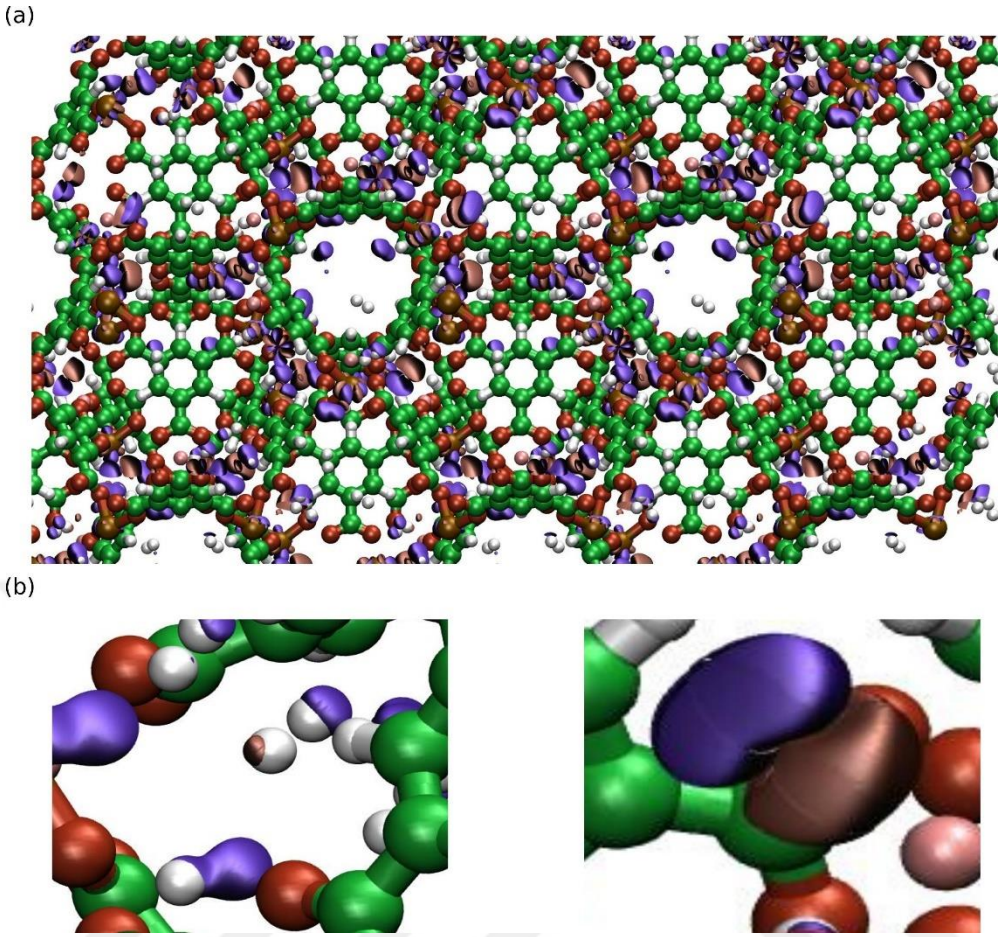

Figure 4.15. (a) Electron density difference calculated for the Fe-Mg-BTC. Isosurfaces taken at + 0.001187 e $Å^{-3}$ for charge accumulation which is represented by pink and -0.001187 e $Å^{-3}$ for charge depletion which is represented by purple (b) Polarizations of H_2 molecules. Fe, Mg, H, O, and C are represented by ochre, pink, white, red and green, respectively.

The Δp(r) calculated for the Cu-Mg-BTC is shown in Figure 4.16 Accumulation and depletion regions are observed on H_2 molecules located next to the Mg atoms and also next to the paddle-wheel unit consisting of Mg and Cu atoms. Polarization is observed on some H_2 molecules. Accumulation and depletion of the paddle-wheel and polarization of the H_2 molecules are depicted detail in Figure 4.16 (b, c).

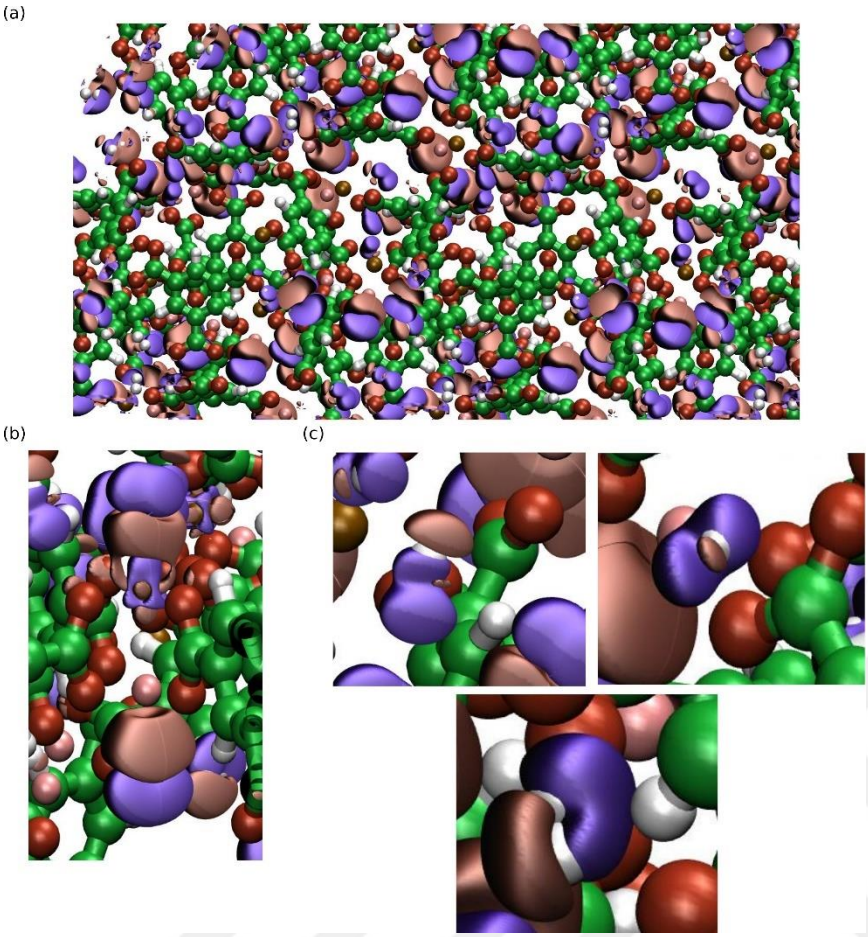

Figure 4.16. (a) Electron density difference calculated for the Cu-Mg-BTC. Isosurfaces taken at +0.00041 e $Å^{-3}$ for charge accumulation which is represented by pink and -0.00041 e $Å^{-3}$ for charge depletion which is represented by purple (b) Electron accumulations and depletions regions located on the paddle-wheel (c) Polarizations of the H_2 molecules. Cu, Mg, H, O, and C are represented by ochre, pink, white, red and green, respectively.

4.4. Frontier Orbital Analysis

In this subsection, we provide the highest occupied molecular orbital (HOMO) and the lowest unoccupied molecular orbital (LUMO) distributions of the selected best performing MM-MOFs.

Figure 4.17 (a, b) shows HOMO and LUMO distributions as computed for the H_2/YOMVIG adsorbed system. Both HOMO and LUMO are located on O and Co atoms of the MM-MOF structure. H_2 molecules do not have any state located on this energy levels.

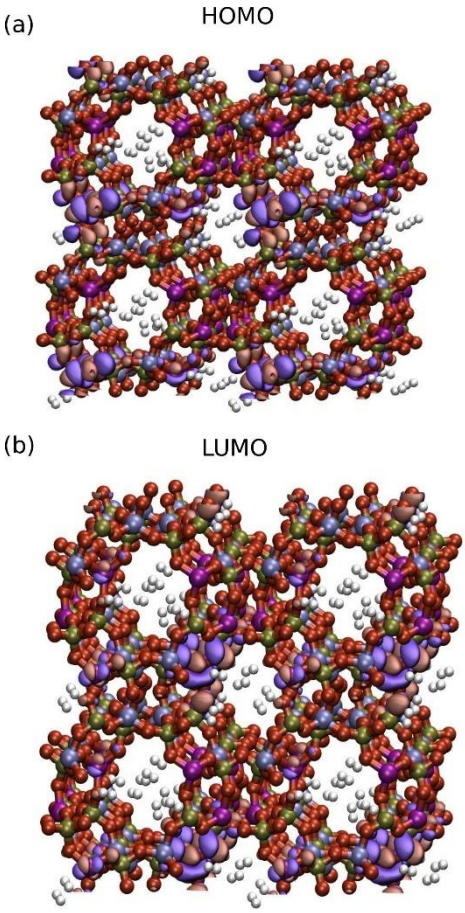

Figure 4.17. a) HOMO and (b) LUMO representations calculated for the H_2/YOMVIG. Isosurfaces are obtained at the value of ± 0.016505 e $Å^{-3}$. Co, P, Al, and O are represented by purple, tan, ice blue and red respectively.

Figure 4.18 shows the HOMO and the LUMO representations computed for the H_2/QIXSOG. HOMO is located on the Mn metal sites and on the ligands connected to the Mn. We observe the similar distribution for the LUMO state. Mn has $3d_{yz}$ orbital. There is no HOMO or LUMO states located on Cu atoms.

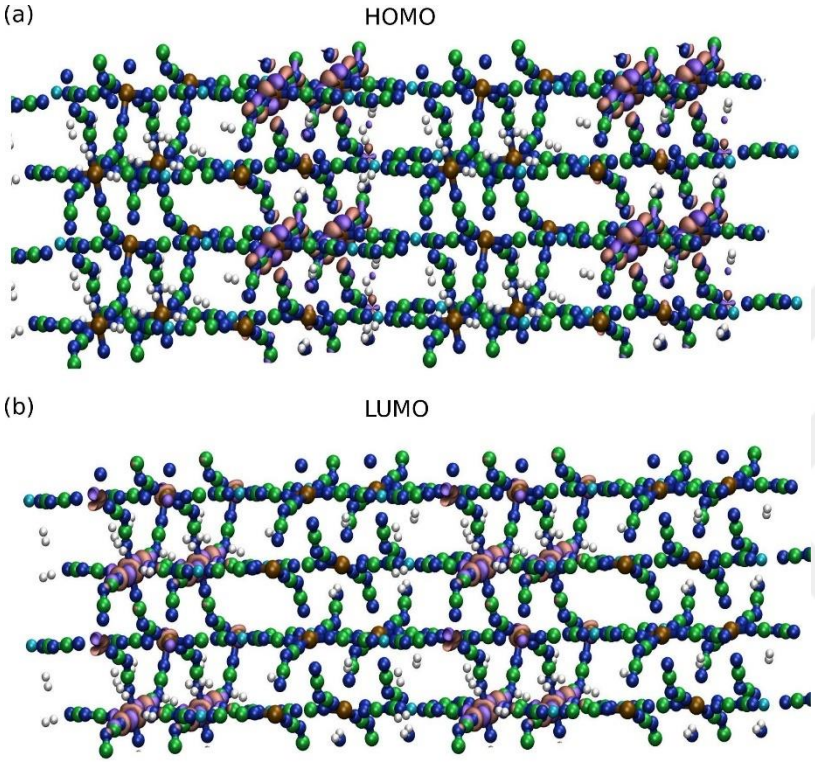

Figure 4.18. a) HOMO and (b) LUMO representations calculated for the H_2/QIXSOG. Isosurfaces are obtained at the value of ± 0.027494 e $Å^{-3}$. Cu, Mn, N and C are represented by cyan, ochre, dark blue and green, respectively.

Figure 4.19 shows the HOMO and the LUMO states of the OSOYUR and adsorbed H_2 molecules. HOMO is located on O, C, and Zn atoms. Ca states do not populate the HOMO. LUMO is distributed on benzene ring, O, and Ca atoms.

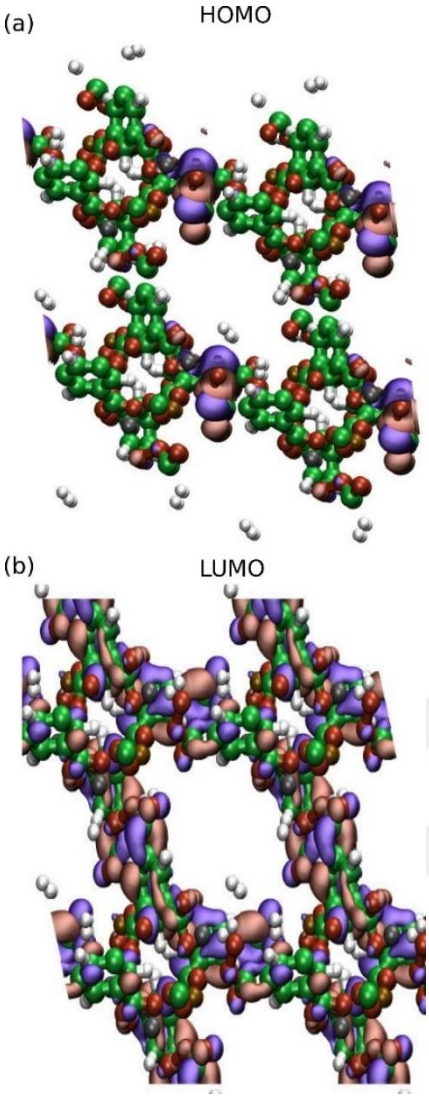

Figure 4.19. a) HOMO and (b) LUMO representations calculated for the H_2/OSOYUR. Isosurfaces are obtained at the value of ± 0.022178 e $Å^{-3}$. Ca, Zn, H, C, and O are represented by ochre, gray, white, green and red, respectively.

Figure 4.20 shows the HOMO and the LUMO states of the Cr-Mg-BTC and H_2 molecules. HOMO is located over Cr and O atoms. Cr $3d_{xy}$ states populates the HOMO. LUMO state is located over benzene ring, Cr, and O.

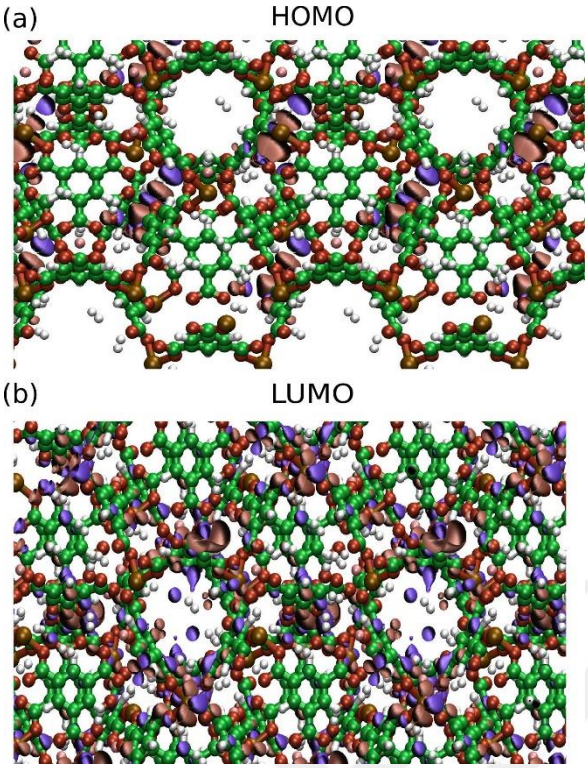

Figure 4.20. a) HOMO and (b) LUMO representations calculated for the H_2//Cr-Mg-BTC. Isosurfaces are obtained at the value of ±0.018 e $Å^{-3}$. Cr, Mg, H, O and C are represented by ochre, pink, white, red and green, respectively.

Figure 4.21 shows the HOMO and LUMO states of the Fe-Mg-BTC and H_2 molecules. HOMO is located on O and Fe atoms where $3d_{yz}$ states of the Fe atoms populates the HOMO. LUMO is distributed over O and Fe atoms.

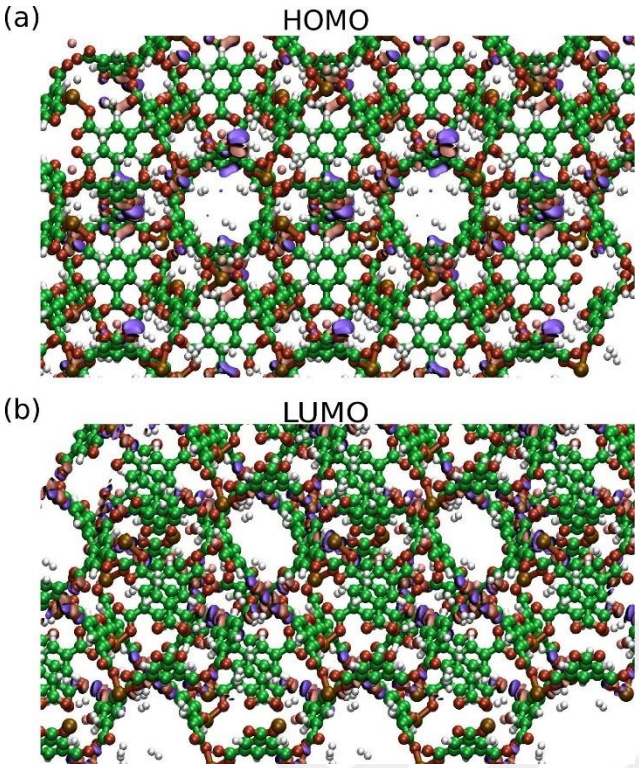

Figure 4.21. a) HOMO and (b) LUMO representations calculated for the H_2//Fe-Mg-BTC. Isosurfaces are obtained at the value of ± 0.021719 e $Å^{-3}$. Fe, Mg, H, O, and C are represented by ochre, pink, white, red, and green, respectively.

Figure 4.22 shows the HOMO and the LUMO states of Cu-Mg-BTC and H_2 molecules. HOMO is located over Cu which has dz^2 orbital. Also, O atoms which has px orbital and is next to Cu is in HOMO state. LUMO is distributed on similar locations with HOMO.

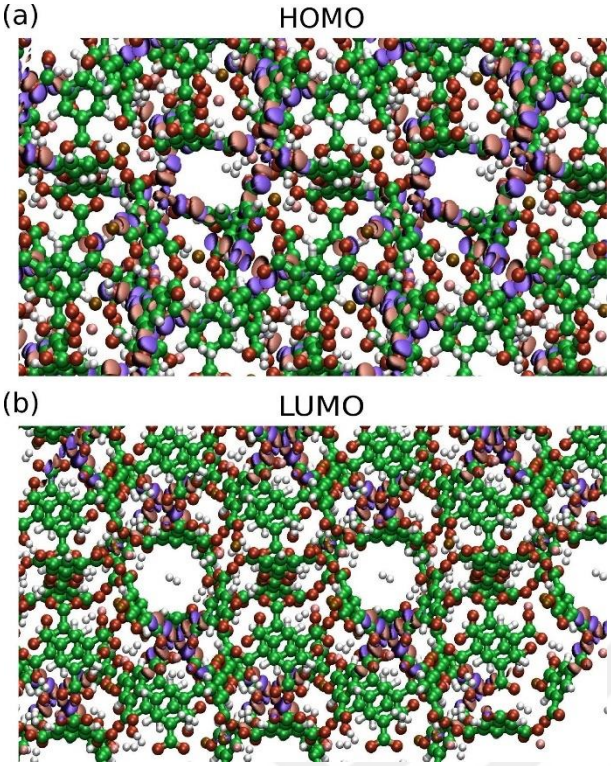

Figure 4.22. a) HOMO and (b) LUMO representations calculated for the H_2//Cu-Mg-BTC. Isosurfaces are obtained at the value of ± 0.018 e $Å^{-3}$. Cu, Mg, H, O and C are represented by ochre, pink, white, red, and green, respectively.

CONCLUSIONS

In this thesis, H_2 adsorption potentials of mixed metal MOFs have been investigated using theoretical approaches such as Grand Canonical Monte Carlo and DFT simulations. We have modeled in total 27 MM-MOFs which are grouped under two categories and their H_2 storage performances have not been investigated so far. Prior to the GCMC simulations which are carried out in order to determine H_2 adsorption isotherms, structures of these MM-MOFs have been optimized applying DFT simulations.

The first group of materials includes totally 15 MM-MOFs which have different chemical and topological properties. The 2nd group of materials composed of 11 hypothetical MM-BTCs which are taken from the study of You et al. (2020). We also added one more material by ourself by combining Co and Mg atoms in the structure of the MM-BTC. Geometry optimization calculations have been carried out only for the Co-Mg-BTC, hypothetical MM-MOF designed by our group, since the rest of the 2nd group materials have been already optimized by You et al. (2020).

H_2 has been modeled using five-site BSS model. MM-BTC structures are assumed to be rigid during the GCMC simulations. We first compared H_2 adsorption results of the GCMC simulations with the available experimental data in the literature carried out for IRMOF-1 and CuBTC. Our simulations agreed well with the experiments, thus we confirm that the BSS model can be used to predict H_2 adsorption isotherms of the MM-MOFs.

H_2 adsorption isotherms and heat of adsorptions have been calculated using GCMC simulations at 233 K and pressure range between 1 and 100 bar. The best H_2 adsorbing materials are determined as YOMVIG, QIXSOG, OSOYUR which belongs to the 1st group materials, and Cu-Mg-BT, Fe-Mg-BTC, and Cr-Mg-BTC which belongs to the 2nd group materials.

Gravimetric and volumetric H_2 uptakes of the 1st group shows large range. 1st group materials have different chemical and topological properties and offers wide variety in terms of the metals sites, PLC, LCD, and void fractions. QIXSOG which has Mn, Cu metal sites and the highest void fraction as well as the LCD among group one and shows the highest gravimetric H_2 adsorption at 100 bar and 233 K which is calculated as 1.53 wt %. H_2 adsorption of the YOMVIG which has Al and Co metal sites performs the top adsorbent as it possesses high volumetric capacity at 233 K and 100 bar, which is calculated as 11.33 g/L. The gravimetric adsorption of the YOMVIG is calculated as 0.58 wt% which also supports that maximizing both gravimetric and volumetric H_2 adsorptions is rather a challenging task. Gravimetric and

volumetric H_2 adsorption of the OSOYUR having Ca and Zn metal sites are calculated as 0.82 wt% and 10.89 g/L, respectively.

Volumetric and gravimetric H_2 adsorption isotherms of 2nd group materials are very close to each other compared to the trend observed in the 1st group materials. The reason is attributed to similarity in topological and chemical properties of these materials. MM-BTCs which have Mg metal sites show the highest gravimetric and volumetric adsorption at 233K and 100 bar. Cu-Mg-BTC shows 1.56 wt % gravimetric and 12.27 g/L volumetric H_2 uptake. Gravimetric and volumetric H_2 adsorption of the Fe-Mg-BTC is calculated as 1.6 wt % and 12.13 g/L, respectively. Cr-Mg-BTC shows 1.64 wt% and 12.24 g/L gravimetric and volumetric H_2 adsorption, respectively.

After evaluating the results of the 2nd group materials, Cr atoms of the Cr-Mg-BTC are replaced with Co atom as it is well known that the presence of the Co metal in framework can increase adsorption of H_2. Gravimetric and volumetric H_2 adsorptions for the Co-Mg-BTC are calculated as 1.58 wt% and 12.01 g/L, respectively. The results of the Co-Mg-BTC are also very similar to the results obtained for the rest of the 2nd group MM-MOFs. Thus, significant improvement of the H_2 adsorption have not been observed by adding Co metals in the structure of the BTCs.

Considering the enthalpies of H_2 adsorption calculated for all the MM-MOFs, enthalpy of adsorption is highly related to the topological features. H_2 interacts stronger with the MM-MOFs having smaller pore sizes. The QIXSOG shows the lowest enthalpy of adsorption (approximately 4 kJ/mol), although it shows the highest gravimetric capacity. This result is attributed to the topology of the QIXSOG which has bridged dca ligands and relatively large PLD and LCD with respect to the other materials listed under the 1st group. WAVWEW having Ba and Co metal sites as well as the smallest LCD (3.41 Å) value shows the greatest enthalpy of adsorption which is calculated as 11 kJ/mol. Additively, WAVWEW shows relatively high volumetric H_2 adsorption which is determined as 10.09 g/L. YOMVIG also shows strong interaction with H_2 having enthalpy of adsorption approximately 10 kJ/mol. YOZJEE and UKULOB01 have 8 kJ/mol and 6 kJ/mol enthalpies of adsorption, although their structures include same kind of atoms. Void fraction, PLD, and LCD values of the YOZJEE are slightly larger than the UKULOB01.

As a general observation, the 1st group materials show higher enthalpies than the 2nd group materials. The calculated enthalpies for the 2nd group materials are very similar with each other and fluctuates around approximately 5 kJ/mol.

The distances between adsorbed H_2 molecules and the metal sites of the MM-MOFs have been measured following geometry optimization of the H_2/MM-MOF systems. A relevant GCMC snapshot is taken from each GCMC simulation of the top performing MM-MOFs which is used as initial coordinates for the geometry optimization simulations. According to the results, H_2 molecules are adsorbed in the close vicinity of the metal sites which results in H_2-metal site distance range from 2 Å to 4 Å. The shortest H_2-metal site distance is observed for the Cr-Mg-BTC which are measured as around 2.2 Å.

Electron density difference analysis and HOMO-LUMO representations are carried out for the best performing MM-MOFs. Electron density difference analysis reveals polarizations of the H_2 molecules for the OSOYUR, Cr-Mg-BTC, Cu-Mg-BTC, and Fe-Mg-BTC.

As a conclusion, there are wide range of researches in literature studying H_2 adsorption on MOFs having single type metal nodes, however studies on H_2 storage potentials of the MOFs having mixed metal nodes have been rarely studied. In this thesis, a wide variety of MM-MOFs having different mixed metals, pore diameters, void fractions, and ligand types have been investigated as H_2 adsorbents. In this way, H_2 storage characteristics of the MM-MOFs have been identified which will be helpful for providing design strategies for future studies.

REFERENCES

A European Green Deal. (n.d.). [Text]. European Commission - European Commission. Retrieved October 11, 2021, from https://ec.europa.eu/info/strategy/priorities-2019-2024/european-green-deal_en

Abe, J. O., Popoola, A. P. I., Ajenifuja, E., & Popoola, O. M. (2019). Hydrogen energy, economy and storage: Review and recommendation. *International Journal of Hydrogen Energy*, *44*(29), 15072–15086.

Abednatanzi, S., Derakhshandeh, P. G., Depauw, H., Coudert, F.-X., Vrielinck, H., Van Der Voort, P., & Leus, K. (2019). Mixed-metal metal–organic frameworks. *Chemical Society Reviews*, *48*(9), 2535–2565.

Allen, M. P., & Tildesley, D. J. (2017). *Computer simulation of liquids*. Oxford university press.

Assoualaye, G., & Djongyang, N. (2021). Influence of pore size and isosteric heat of adsorption of some metal–organic frameworks on the volumetric and gravimetric adsorption capacities of hydrogen at room temperature. *Polymer Bulletin*, *78*(9), 4987–5001.

Assoualaye, G., Tom, A., & Djongyang, N. (2020). Monte carlo study of hydrogen adsorption by MOF-5 doped with cobalt at ambient temperature and pressure. *SN Applied Sciences*, *2*(11), 1–10.

Atkins, P., & De Paula, J. (2011). *Physical chemistry for the life sciences*. Oxford University Press, USA.

Basdogan, Y., & Keskin, S. (2015). Simulation and modelling of MOFs for hydrogen storage. *CrystEngComm*, *17*(2), 261–275.

Belof, J. L., Stern, A. C., & Space, B. (2008). An accurate and transferable intermolecular diatomic hydrogen potential for condensed phase simulation. *Journal of Chemical Theory and Computation*, *4*(8), 1332–1337.

Bhatia, S. K., & Myers, A. L. (2006). Optimum conditions for adsorptive storage. *Langmuir*, *22*(4), 1688–1700.

Bloomberg. (n.d.). Retrieved April 21, 2022, from https://www.bloomberg.com/news/articles/2021-09-08/this-village-in-england-is-already-using-hydrogen-to-heat-homes

Bobbitt, N. S., Chen, J., & Snurr, R. Q. (2016). High-Throughput Screening of Metal–Organic Frameworks for Hydrogen Storage at Cryogenic Temperature. *The Journal of Physical Chemistry C*, *120*(48), 27328–27341. https://doi.org/10.1021/acs.jpcc.6b08729

Boese, A. D., Doltsinis, N. L., Handy, N. C., & Sprik, M. (2000). New generalized gradient approximation functionals. *The Journal of Chemical Physics*, *112*(4), 1670–1678.

Borboudakis, G., Stergiannakos, T., Frysali, M., Klontzas, E., Tsamardinos, I., & Froudakis, G. E. (2017). Chemically intuited, large-scale screening of MOFs by machine learning techniques. *Npj Computational Materials*, *3*(1), 1–7.

Botas, J. A., Calleja, G., Sánchez-Sánchez, M., & Orcajo, M. G. (2010). Cobalt doping of the MOF-5 framework and its effect on gas-adsorption properties. *Langmuir*, *26*(8), 5300–5303.

Botas, J. A., Calleja, G., Sanchez-Sanchez, M., & Orcajo, M. G. (2011). Effect of Zn/Co ratio in MOF-74 type materials containing exposed metal sites on their hydrogen adsorption behaviour and on their band gap energy. *International Journal of Hydrogen Energy*, *36*(17), 10834–10844.

Clark, J. (n.d.). *Mercedes-Benz F125! Research Vehicle Technology | eMercedesBenz*. Retrieved October 19, 2021, from https://emercedesbenz.com/autos/mercedes-benz/concept-vehicles/mercedes-benz-f125-research-vehicle-technology/

Collins, D. J., & Zhou, H.-C. (2007). Hydrogen storage in metal–organic frameworks. *Journal of Materials Chemistry*, *17*(30), 3154–3160.

Dantu, S. C. (2012). *Conformational sampling of enzyme dynamics: Triosephosphate isomerase.* [PhD Thesis]. Georg-August-Universität Göttingen.

Dinca, M., & Long, J. R. (2007). High-enthalpy hydrogen adsorption in cation-exchanged variants of the microporous metal- organic framework Mn3 [(Mn4Cl) 3 (BTT) 8 (CH3OH) 10] 2. *Journal of the American Chemical Society*, *129*(36), 11172–11176.

DOE Technical Targets for Onboard Hydrogen Storage for Light-Duty Vehicles. (n.d.). Energy.Gov. Retrieved March 8, 2021, from https://www.energy.gov/eere/fuelcells/doe-technical-targets-onboard-hydrogen-storage-light-duty-vehicles

Dubbeldam, D., Calero, S., Ellis, D. E., & Snurr, R. Q. (2016). RASPA: Molecular simulation software for adsorption and diffusion in flexible nanoporous materials. *Molecular Simulation*, *42*(2), 81–101.

Düren, T., Bae, Y.-S., & Snurr, R. Q. (2009). Using molecular simulation to characterise metal–organic frameworks for adsorption applications. *Chemical Society Reviews*, *38*(5), 1237–1247.

Durette, D., Bénard, P., Zacharia, R., & Chahine, R. (2016). Investigation of the hydrogen adsorbed density inside the pores of MOF-5 from path integral grand canonical Monte Carlo at supercritical and subcritical temperature. *Science Bulletin*, *61*(8), 594–600.

Férey, G., Latroche, M., Serre, C., Millange, F., Loiseau, T., & Percheron-Guégan, A. (2003). Hydrogen adsorption in the nanoporous metal-benzenedicarboxylate M(OH)(O2C–C6H4–CO2)(M = Al3+, Cr3+), MIL-53. *Chemical Communications*, *24*, 2976–2977. https://doi.org/10.1039/B308903G

Franz, D. M., Dyott, Z. E., Forrest, K. A., Hogan, A., Pham, T., & Space, B. (2018). Simulations of hydrogen, carbon dioxide, and small hydrocarbon sorption in a nitrogen-rich rht-metal–organic framework. *Physical Chemistry Chemical Physics*, *20*(3), 1761–1777.

Frenkel, D. (2004). Introduction to monte carlo methods. *NIC Series*, *23*, 29–60.

Frost, H., Düren, T., & Snurr, R. Q. (2006). Effects of surface area, free volume, and heat of adsorption on hydrogen uptake in metal- organic frameworks. *The Journal of Physical Chemistry B*, *110*(19), 9565–9570.

Furukawa, H., Cordova, K. E., O'Keeffe, M., & Yaghi, O. M. (2013). The chemistry and applications of metal-organic frameworks. *Science*, *341*(6149).

Getman, R. B., Bae, Y.-S., Wilmer, C. E., & Snurr, R. Q. (2012). Review and analysis of molecular simulations of methane, hydrogen, and acetylene storage in metal–organic frameworks. *Chemical Reviews*, *112*(2), 703–723.

Goedecker, S., Teter, M., & Hutter, J. (1996). Separable dual-space Gaussian pseudopotentials. *Physical Review B*, *54*(3), 1703.

Grimme, S., Antony, J., Ehrlich, S., & Krieg, H. (2010). A consistent and accurate ab initio parametrization of density functional dispersion correction (DFT-D) for the 94 elements H-Pu. *The Journal of Chemical Physics*, *132*(15), 154104.

Gürdal, Y. (2013). *Computing adsorption, diffusion and separation of noble gas mixtures in MOFs using molecular simulations and theoretical correlations* [Master's thesis, Koc University]. https://tez.yok.gov.tr/UlusalTezMerkezi/tezDetay.jsp?id=Py_O7naAA-NRJqCVw11S5w&no=37EtHO679IqRBU-PyyJy_A

Gürdal, Y. (2017). *Theoretical Investigation of H2 Generation Systems: From Homogenous to Heterogeneous Photo-Catalysis* [PhD Thesis]. University of Zurich.

Gurdal, Y., & Iannuzzi, M. (2017). DFT-based Theoretical simulations for photocatalytic applications using TiO2. *Titanium Dioxide*, 189.

Gurdal, Y., & Keskin, S. (2012). Atomically detailed modeling of metal organic frameworks for adsorption, diffusion, and separation of noble gas mixtures. *Industrial & Engineering Chemistry Research*, *51*(21), 7373–7382.

Han, S. S., Deng, W.-Q., & Goddard III, W. A. (2007). Improved designs of metal–organic frameworks for hydrogen storage. *Angewandte Chemie*, *119*(33), 6405–6408.

Han, S. S., & Goddard, W. A. (2007). Lithium-doped metal-organic frameworks for reversible H2 storage at ambient temperature. *Journal of the American Chemical Society*, *129*(27), 8422–8423.

Han, S. S., Mendoza-Cortés, J. L., & Goddard Iii, W. A. (2009). Recent advances on simulation and theory of hydrogen storage in metal–organic frameworks and covalent organic frameworks. *Chemical Society Reviews*, *38*(5), 1460–1476.

Hidrojen Yakıtlı Toyota Mirai'den Dünya Menzil Rekoru. (n.d.). Retrieved October 26, 2021, from https://www.toyota.com.tr/world-of-toyota/news/Hidrojen-Yakitli-Toyota-Mirai-den-Dunya-Menzil-Rekoru.json

Hirscher, M., & Panella, B. (2007). Hydrogen storage in metal–organic frameworks. *Scripta Materialia*, *56*(10), 809–812.

Hu, Y. H., & Zhang, L. (2010). Hydrogen storage in metal–organic frameworks. *Advanced Materials*, *22*(20), E117–E130.

HyDeploy. (n.d.). HyDeploy. Retrieved April 21, 2022, from https://hydeploy.co.uk/about/

Hydrogen and Fuel Cell Technologies Office. (n.d.). Energy.Gov. Retrieved March 8, 2021, from https://www.energy.gov/eere/fuelcells/hydrogen-storage

Hydrogen Storage. (n.d.). Energy.Gov. Retrieved November 15, 2021, from https://www.energy.gov/eere/fuelcells/hydrogen-storage

Hydrogen strategy. (n.d.). Retrieved October 11, 2021, from https://ec.europa.eu/energy/sites/ener/files/hydrogen_strategy.pdf

Ino, S., Sato, M., Hosono, M., & Izumi, T. (2009). Development of a soft metal hydride actuator using a laminate bellows for rehabilitation systems. *Sensors and Actuators B: Chemical*, *136*(1), 86–91.

Jain, I. P. (2009). Hydrogen the fuel for 21st century. *International Journal of Hydrogen Energy*, *34*(17), 7368–7378.

Kapelewski, M. T., Runčevski, T., Tarver, J. D., Jiang, H. Z., Hurst, K. E., Parilla, P. A., Ayala, A., Gennett, T., FitzGerald, S. A., & Brown, C. M. (2018). Record high hydrogen storage capacity in the metal–organic framework Ni2 (m-dobdc) at near-ambient temperatures. *Chemistry of Materials*, *30*(22), 8179–8189.

Kaur, G., Rai, R. K., Tyagi, D., Yao, X., Li, P.-Z., Yang, X.-C., Zhao, Y., Xu, Q., & Singh, S. K. (2016). Room-temperature synthesis of bimetallic Co–Zn based zeolitic imidazolate

frameworks in water for enhanced CO 2 and H 2 uptakes. *Journal of Materials Chemistry A*, *4*(39), 14932–14938.

Kaye, S. S., Dailly, A., Yaghi, O. M., & Long, J. R. (2007). Impact of preparation and handling on the hydrogen storage properties of Zn4O (1, 4-benzenedicarboxylate) 3 (MOF-5). *Journal of the American Chemical Society*, *129*(46), 14176–14177.

Kohn, W., Becke, A. D., & Parr, R. G. (1996). Density functional theory of electronic structure. *The Journal of Physical Chemistry*, *100*(31), 12974–12980.

Koizumi, K., Nobusada, K., & Boero, M. (2019). Hydrogen storage mechanism and diffusion in metal–organic frameworks. *Physical Chemistry Chemical Physics*, *21*(15), 7756–7764.

Kökçam-Demir, Ü., Goldman, A., Esrafili, L., Gharib, M., Morsali, A., Weingart, O., & Janiak, C. (2020). Coordinatively unsaturated metal sites (open metal sites) in metal–organic frameworks: Design and applications. *Chemical Society Reviews*, *49*(9), 2751–2798.

Kosa, M., Krack, M., Cheetham, A. K., & Parrinello, M. (2008). Modeling the hydrogen storage materials with exposed M2+ coordination sites. *The Journal of Physical Chemistry C*, *112*(42), 16171–16173.

Kumar, R., Moshi, A. A. M., Bharathi, S. S., Dhanasekaran, C., Sivaganesan, S., Senthamaraikannan, P., Saravanakumar, S. S., & Khan, A. (2020). Significance of Metal-Organic Frameworks Consisting of Porous Materials. In *Metal-Organic Framework Nanocomposites* (pp. 1–12). CRC Press.

Kushch, N. D., Kazakova, A. V., Dubrovskii, A. D., Shilov, G. V., Buravov, L. I., Morgunov, R. B., Kurganova, E. V., Tanimoto, Y., & Yagubskii, E. B. (2007). Molecular magnetic semiconductors formed by cationic and anionic networks:(ET) 2 Mn [N (CN) 2] 3 and (ET) 2 CuMn [N (CN) 2] 4. *Journal of Materials Chemistry*, *17*(41), 4407–4413.

Lai, Q., Paskevicius, M., Sheppard, D. A., Buckley, C. E., Thornton, A. W., Hill, M. R., Gu, Q., Mao, J., Huang, Z., & Liu, H. K. (2015). Hydrogen storage materials for mobile and stationary applications: Current state of the art. *ChemSusChem*, *8*(17), 2789–2825.

Li, H., Wang, K., Sun, Y., Lollar, C. T., Li, J., & Zhou, H.-C. (2018). Recent advances in gas storage and separation using metal–organic frameworks. *Materials Today*, *21*(2), 108–121.

Li, J., Cheng, S., Zhao, Q., Long, P., & Dong, J. (2009). Synthesis and hydrogen-storage behavior of metal–organic framework MOF-5. *International Journal of Hydrogen Energy*, *34*(3), 1377–1382.

Li, X., Yang, X., Xue, H., Pang, H., & Xu, Q. (2020). Metal–organic frameworks as a platform for clean energy applications. *EnergyChem*, *2*(2), 100027.

Li, Y., & Yang, R. T. (2008). Hydrogen storage in metal-organic and covalent-organic frameworks by spillover. *AIChE Journal*, *54*(1), 269–279.

Limas, N. G., & Manz, T. A. (2018). Introducing DDEC6 atomic population analysis: Part 4. Efficient parallel computation of net atomic charges, atomic spin moments, bond orders, and more. *RSC Advances*, *8*(5), 2678–2707.

Lin, X., Jia, J., Champness, N. R., Hubberstey, P., & Schröder, M. (2008). Metal-organic framework materials for hydrogen storage. In *Solid-State Hydrogen Storage* (pp. 288–312). Elsevier.

Lin, X.-M., Li, T.-T., Wang, Y.-W., Zhang, L., & Su, C.-Y. (2012). Two ZnII Metal-Organic Frameworks with Coordinatively Unsaturated Metal Sites: Structures, Adsorption, and Catalysis. *Chemistry–An Asian Journal*, *7*(12), 2796–2804.

Lippert, B. G., PARRINELLO, J. H., & MICHELE. (1997). A hybrid Gaussian and plane wave density functional scheme. *Molecular Physics*, *92*(3), 477–488.

Liu, Z., Zhang, L., & Sun, D. (2020). Stimuli-responsive structural changes in metal–organic frameworks. *Chemical Communications*, *56*(66), 9416–9432.

Lochan, R. C., & Head-Gordon, M. (2006). Computational studies of molecular hydrogen binding affinities: The role of dispersion forces, electrostatics, and orbital interactions. *Physical Chemistry Chemical Physics*, *8*(12), 1357–1370.

Lu, J., & Ding, F. (2020). *Nanoporous Materials for Molecule Separation and Conversion*. Elsevier.

Ma, S., Eckert, J., Forster, P. M., Yoon, J. W., Hwang, Y. K., Chang, J.-S., Collier, C. D., Parise, J. B., & Zhou, H.-C. (2008). Further investigation of the effect of framework catenation on hydrogen uptake in metal- organic frameworks. *Journal of the American Chemical Society*, *130*(47), 15896–15902.

Ma, S., Sun, D., Ambrogio, M., Fillinger, J. A., Parkin, S., & Zhou, H.-C. (2007). Framework-catenation isomerism in metal- organic frameworks and its impact on hydrogen uptake. *Journal of the American Chemical Society*, *129*(7), 1858–1859.

Manz, T. A., & Sholl, D. S. (2010). Chemically meaningful atomic charges that reproduce the electrostatic potential in periodic and nonperiodic materials. *Journal of Chemical Theory and Computation*, *6*(8), 2455–2468.

Masika, E., & Mokaya, R. (2012). Hydrogen storage in high surface area carbons with identical surface areas but different pore sizes: Direct demonstration of the effects of pore size. *The Journal of Physical Chemistry C*, *116*(49), 25734–25740.

Masoomi, M. Y., Morsali, A., Dhakshinamoorthy, A., & Garcia, H. (2019). Mixed-metal MOFs: Unique opportunities in metal–organic framework (MOF) functionality and design. *Angewandte Chemie*, *131*(43), 15330–15347.

Metal Organic Framework Database | Mofs. (n.d.). Retrieved August 29, 2021, from https://mof.tech.northwestern.edu/

Metropolis, N., Rosenbluth, A. W., Rosenbluth, M. N., Teller, A. H., & Teller, E. (1953). Equation of state calculations by fast computing machines. *The Journal of Chemical Physics*, *21*(6), 1087–1092.

Montes-Andres, H., Orcajo, G., Martos, C., Botas, J. A., & Calleja, G. (2019). Co/Ni mixed-metal expanded IRMOF-74 series and their hydrogen adsorption properties. *International Journal of Hydrogen Energy*, *44*(33), 18205–18213.

Nazir, H., Muthuswamy, N., Louis, C., Jose, S., Prakash, J., Buan, M. E., Flox, C., Chavan, S., Shi, X., & Kauranen, P. (2020). Is the H2 economy realizable in the foreseeable future? Part II: H2 storage, transportation, and distribution. *International Journal of Hydrogen Energy*.

Niaz, S., Manzoor, T., & Pandith, A. H. (2015). Hydrogen storage: Materials, methods and perspectives. *Renewable and Sustainable Energy Reviews*, *50*, 457–469.

Nikolaidis, P., & Poullikkas, A. (2017). A comparative overview of hydrogen production processes. *Renewable and Sustainable Energy Reviews*, *67*, 597–611.

NIST/ARPA-E Database of Novel and Emerging Adsorbent Materials. (n.d.). Retrieved June 21, 2022, from https://adsorption.nist.gov/isodb/index.php?DOI=10.1002/adfm.200500561#home

Ongari, D., Tiana, D., Stoneburner, S. J., Gagliardi, L., & Smit, B. (2017). Origin of the Strong Interaction between Polar Molecules and Copper (II) Paddle-Wheels in Metal Organic Frameworks. *The Journal of Physical Chemistry C*, *121*(28), 15135–15144.

Panella, B., Hirscher, M., Pütter, H., & Müller, U. (2006). Hydrogen adsorption in metal–organic frameworks: Cu-MOFs and Zn-MOFs compared. *Advanced Functional Materials*, *16*(4), 520–524.

Park, N., Choi, K., Hwang, J., Kim, D. W., Kim, D. O., & Ihm, J. (2012). Progress on first-principles-based materials design for hydrogen storage. *Proceedings of the National Academy of Sciences*, *109*(49), 19893–19899.

Peedikakkal, A. M. P., & Aljundi, I. H. (2020). Mixed-Metal Cu-BTC Metal–Organic Frameworks as a Strong Adsorbent for Molecular Hydrogen at Low Temperatures. *ACS Omega*, *5*(44), 28493–28499.

Peedikakkal, A. M. P., & Aljundi, I. H. (2021). Upgrading the Hydrogen Storage of MOF-5 by Post-Synthetic Exchange with Divalent Metal Ions. *Applied Sciences*, *11*(24), 11687.

Perdew, J. P., Burke, K., & Ernzerhof, M. (1996). Generalized gradient approximation made simple. *Physical Review Letters*, *77*(18), 3865.

Rappé, A. K., Casewit, C. J., Colwell, K. S., Goddard III, W. A., & Skiff, W. M. (1992). UFF, a full periodic table force field for molecular mechanics and molecular dynamics simulations. *Journal of the American Chemical Society*, *114*(25), 10024–10035.

Rosi, N. L., Eckert, J., Eddaoudi, M., Vodak, D. T., Kim, J., O'Keeffe, M., & Yaghi, O. M. (2003). Hydrogen storage in microporous metal-organic frameworks. *Science*, *300*(5622), 1127–1129.

Rowsell, J. L., Millward, A. R., Park, K. S., & Yaghi, O. M. (2004). Hydrogen sorption in functionalized metal- organic frameworks. *Journal of the American Chemical Society*, *126*(18), 5666–5667.

Rowsell, J. L., & Yaghi, O. M. (2005). Strategies for hydrogen storage in metal–organic frameworks. *Angewandte Chemie International Edition*, *44*(30), 4670–4679.

Ryan, P., Broadbelt, L. J., & Snurr, R. Q. (2008). Is catenation beneficial for hydrogen storage in metal–organic frameworks? *Chemical Communications*, *35*, 4132–4134.

Sagara, T., Klassen, J., & Ganz, E. (2004). Computational study of hydrogen binding by metal-organic framework-5. *The Journal of Chemical Physics*, *121*(24), 12543–12547.

Sagara, T., Klassen, J., Ortony, J., & Ganz, E. (2005). Binding energies of hydrogen molecules to isoreticular metal-organic framework materials. *The Journal of Chemical Physics*, *123*(1), 014701.

Sasaki, T., Kawashima, T., Aoyama, H., Ogawa, T., & Ifukube, T. (1987). Development of an actuator using a metal hydride and its application to a lifter for the disabled. *Advanced Robotics*, *2*(3), 277–286.

Schoenung, S. (2011). Economic analysis of large-scale hydrogen storage for renewable utility applications. *International Colloquium on Environmentally Preferred Advanced Power Generation*, 8e10.

Song, X., Li, J., Guo, Y., Pan, Q., Gan, L., Yu, J., & Xu, R. (2009). Syntheses and characterizations of transition-metal-substituted aluminophosphate molecular sieves|(C3N2H5) 8|[M8Al16P24O96](M= Co, Mn, Zn) with zeotype LAU topology. *Inorganic Chemistry*, *48*(1), 198–203.

Suh, M. P., Park, H. J., Prasad, T. K., & Lim, D.-W. (2012). Hydrogen storage in metal–organic frameworks. *Chemical Reviews*, *112*(2), 782–835.

Sule, R., Mishra, A. K., & Nkambule, T. T. (2021). Recent advancement in consolidation of MOFs as absorbents for hydrogen storage. *International Journal of Energy Research*, *45*(9), 12481–12499.

Sun, Y. Y., Kim, Y.-H., & Zhang, S. B. (2007). Effect of spin state on the dihydrogen binding strength to transition metal centers in metal-organic frameworks. *Journal of the American Chemical Society*, *129*(42), 12606–12607.

Torres, N., Galicia, J., Plasencia, Y., Cano, A., Echevarría, F., Desdin-Garcia, L. F., & Reguera, E. (2018). Implications of structural differences between Cu-BTC and Fe-BTC on their hydrogen storage capacity. *Colloids and Surfaces A: Physicochemical and Engineering Aspects*, *549*, 138–146.

United Nations Department of Economic and Social Affairs. (n.d.). Retrieved November 4, 2021, from https://www.un.org/development/desa/en/news/population/world-population-prospects-2019.html

Van Voorhis, T., & Scuseria, G. E. (1998). A novel form for the exchange-correlation energy functional. *The Journal of Chemical Physics*, *109*(2), 400–410.

VandeVondele, J., & Hutter, J. (2007). Gaussian basis sets for accurate calculations on molecular systems in gas and condensed phases. *The Journal of Chemical Physics*, *127*(11), 114105.

VandeVondele, J., Krack, M., Mohamed, F., Parrinello, M., Chassaing, T., & Hutter, J. (2005). Quickstep: Fast and accurate density functional calculations using a mixed Gaussian and plane waves approach. *Computer Physics Communications*, *167*(2), 103–128.

Villajos, J. A., Orcajo, G., Martos, C., Botas, J. Á., Villacañas, J., & Calleja, G. (2015). Co/Ni mixed-metal sited MOF-74 material as hydrogen adsorbent. *International Journal of Hydrogen Energy*, *40*(15), 5346–5352.

Wakisaka, Y., Mure, M., Kabutomori, T., Takeda, H., Shimizu, S., Ino, S., & Ifukube, T. (1997). Application of hydrogen absorbing alloys to medical and rehabilitation equipment. *IEEE Transactions on Rehabilitation Engineering*, *5*(2), 148–157.

Wang, L., Wang, L., Zhao, J., & Yan, T. (2012). Adsorption of selected gases on metal-organic frameworks and covalent organic frameworks: A comparative grand canonical Monte Carlo simulation. *Journal of Applied Physics*, *111*(11), 112628.

Willems, T. F., Rycroft, C. H., Kazi, M., Meza, J. C., & Haranczyk, M. (2012). Algorithms and tools for high-throughput geometry-based analysis of crystalline porous materials. *Microporous and Mesoporous Materials*, *149*(1), 134–141.

Winarta, J., Yung, A., & Mu, B. (2020). Hydrogen and methane storage in nanoporous materials. In *Nanoporous Materials for Molecule Separation and Conversion* (pp. 327–350). Elsevier.

Wong-Foy, A. G., Matzger, A. J., & Yaghi, O. M. (2006). Exceptional H2 saturation uptake in microporous metal- organic frameworks. *Journal of the American Chemical Society*, *128*(11), 3494–3495.

Yang, Q., & Zhong, C. (2006). Understanding hydrogen adsorption in metal- organic frameworks with open metal sites: A computational study. *The Journal of Physical Chemistry B*, *110*(2), 655–658.

Yang, S. J., Jung, H., Kim, T., Im, J. H., & Park, C. R. (2012). Effects of structural modifications on the hydrogen storage capacity of MOF-5. *International Journal of Hydrogen Energy*, *37*(7), 5777–5783.

You, W., Liu, Y., Howe, J. D., Tang, D., & Sholl, D. S. (2018). Tuning binding tendencies of small molecules in metal–organic frameworks with open metal sites by metal substitution and linker functionalization. *The Journal of Physical Chemistry C*, *122*(48), 27486–27494.

You, W., Sen, T., Kawajiri, Y., Realff, M. J., & Sholl, D. S. (2020). Using Site Heterogeneity in Metal–Organic Frameworks with Bimetallic Open Metal Sites for Olefin/Paraffin Separations. *ACS Applied Nano Materials*, *3*(6), 5291–5300.

You-Kwan, O., Subramanian, M. R., Gyoo, Y. J., & Sunghoon, P. (2013). Chapter 3-Metabolic Engineering of Microorganisms for Biohydrogen Production. *Biohydrogen, Edited by Ashok Pandey, Jo-Shu Chang, Patrick C. Hallenbecka and Christian Larroche, Elsevier., Amsterdam*, 45–65.

Yusaf, T., Laimon, M., Alrefae, W., Kadirgama, K., Dhahad, H. A., Ramasamy, D., Kamarulzaman, M. K., & Yousif, B. (2022). Hydrogen Energy Demand Growth Prediction and Assessment (2021–2050) Using a System Thinking and System Dynamics Approach. *Applied Sciences*, *12*(2), 781.

Zeleňák, V., & Saldan, I. (2021). Factors Affecting Hydrogen Adsorption in Metal–Organic Frameworks: A Short Review. *Nanomaterials*, *11*(7), 1638.

Zhang, H., Bucior, B. J., & Snurr, R. Q. (2018). Molecular modeling of carbon dioxide adsorption in metal-organic frameworks. In *Modelling and Simulation in the Science of Micro- and Meso-Porous Materials* (pp. 99–149). Elsevier.

Zoellter, J. (2011, September 13). *Mercedes-Benz F125 Concept*. Car and Driver. https://www.caranddriver.com/photos/g18120954/mercedes-benz-f125-concept-gallery

Zohuri, B. (2018). Hydrogen energy technology, renewable source of energy. In *Hybrid Energy Systems* (pp. 135–179). Springer.

Zou, R., Zhong, R., Han, S., Xu, H., Burrell, A. K., Henson, N., Cape, J. L., Hickmott, D. D., Timofeeva, T. V., & Larson, T. E. (2010). A Porous Metal- Organic Replica of α-PbO2 for Capture of Nerve Agent Surrogate. *Journal of the American Chemical Society*, *132*(51), 17996–17999.